Numerical simulation and design of semiconductor quantum dot-based lasers and amplifiers

more. The coupling between the forward and backward pulses will be weaker in the middle of the device and becomes stronger again when approaching the gain section side facet.

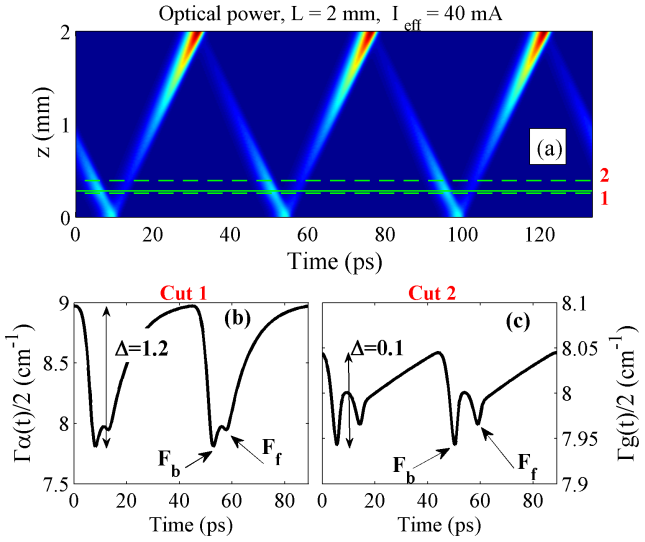

Figure 3.13: (a) Spatio-temporal evolution of the GS optical power inside the laser cavity of device A when $I_{eff} = 40$ mA. The horizontal solid line indicates the separation between the SA and the gain section. The horizontal dashed lines represent two cuts in the laser cavity, one in the SA (1) and another gain section (2). The corresponding temporal evolution of the modal absorption and gain for the optical field at these two cuts are shown in (b) and (c) respectively.

Comparing Figs. 3.13b and 3.13c, one can clearly observe a big difference between the maximum absorption bleaching and the maximum gain compression. Since the optical field power in these two close cuts should be similar, above observation confirms our expectation that gain section is harder to be saturated than the SA.

In the following, we will show directly the pulse energy evolution in the laser cavity, which is computed by the integration over time of the optical power of a pulse when it forward or backward crosses the considered section of the cavity (labelled as $E_f(z)$ and $E_b(z)$). Besides, it is shown also the local net modal gain ($G(z)$) distribution in both directions. For the forward propagation, $G(z)$ is calculated as $\ln[E_f(z + \Delta z) \ / \ E_f(z)] \ / \ \Delta z$, while for the backward propagation, it is calculated as $\ln[E_b(z - \Delta z) \ / \ E_b(z)] \ / \ \Delta z$, being Δz the spatial simulation step. $|G(z)|$ when $G(z) < 0$ represents the modal absorption.

A. Change of L_{SA} and R_L

Keeping the same total length of 2 mm, ML has been investigated for devices with SA length of 287, 380, 467, 533 and 590 μm, equivalent to the absorber-to-total length ratio (L_{SA}/L) of 1:7, 1:5.3, 1:4.3, 1:3.75 and 1:3.4 (named as device A, B, C, D, E), and in order to have the same g_{th}, corresponding R_L are assumed to be 4.2%, 8%, 14%, 22% and 33%.

The analysis has been done in a current range of 200 mA starting from I_{eff} = 20 mA and increasing it with a step of 20 mA as shown in Figs. 3.14a) (figures 3.16a, 3.16b and 3.16c are shown in the same way). Consistently with findings in [89], we can see that the pulse width decreases with increasing the SA length (Fig. 3.14a).

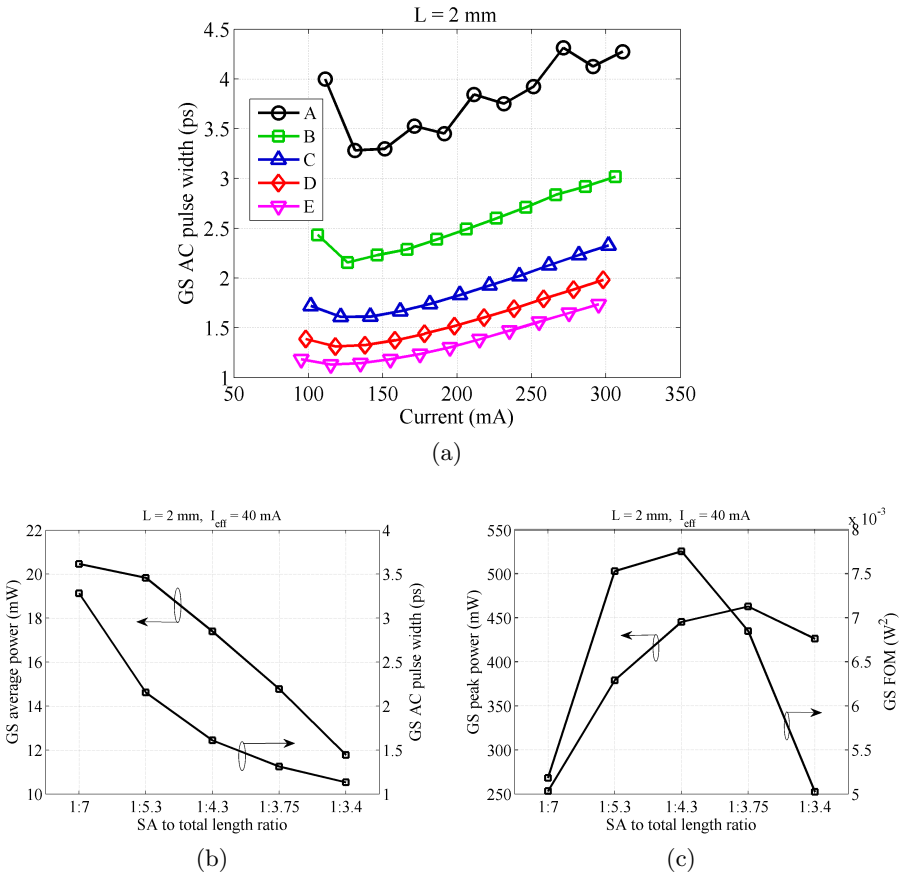

Figure 3.14: (a) Deconvoluted autocorrelation (AC) pulse width as a function of the injection current for the considered five devices A (square), B (circle), C (upward-pointing triangle), D (diamond) and E (downward-pointing triangle). For the same devices, the average power and the AC pulse width (b), the peak power and the FOM (c) are shown as a function of the absorber-to-total length ratio at fixed I_{eff}.

Details of the pulse performances in terms of the average power, the

pulse width, the peak power and the FOM at a fixed I_{eff} are shown in Figs. 3.14b and 3.14c. One can easily find a significant reduction in both the average power and the pulse width when increasing L_{SA}/L. The variation of these two quantities leads to an optimum L_{SA}/L that could achieve the highest peak power or FOM.

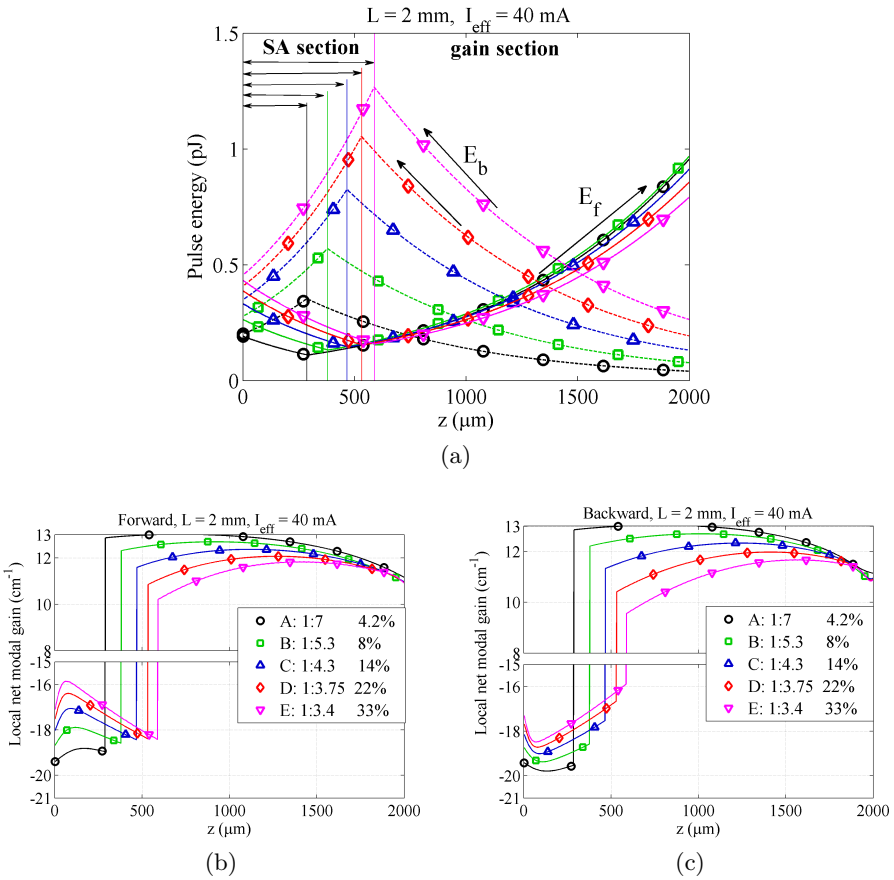

Figure 3.15: For devices in Fig. 3.14, at the same I_{eff}, show also the evolution of the intracavity PE (a) (solid and dashed lines are for forward and backward propagations respectively), and the local net modal gain/absorption when the pulse is forward (b) or backward (c) propagating in the cavity. Devices are distinguished always with the same markers as in Fig. 3.14a. In (a), the straight vertical lines indicate the separation between the SA and the gain section. In (b) and (c) the ordinate range limits correspond to the unsaturated gain and absorption values.

In principle, stable ML with identical energy for each pulse results from the self-consistent solution of the ML system which balances the amplification in the gain section, the attenuation in the SA and the boundary conditions of the reflectivities at both facets. From Fig. 3.15a it is evident that, since device with longer SA would lead to larger total PE attenuation in the SA, the self-consistent ML established in such device must have higher

intra-SA PE to compensate this large attenuation.

Furthermore, after experiencing a continuous attenuation in the SA, the forward propagating pulses in all the devices reach a point where E_f is almost the same for all the pulses ($z = 590$ μm). Beyond this point, differences in E_f start to emerge. and this can be attributed to the differences in the forward local gain of the pulse. As we can see, due to the strong coupling between the forward and backward pulses, device E which has highest E_b exhibits lowest forward local gain (see Fig. 3.15b), and consequently obtains the lowest E_f at the output facet. This result combined with low power extraction from the output facet due to high R_L explains the smallest average power obtained in device E.

In Figs. 3.15b and 3.15c, we show the evolution of $G(z)$ when the pulse is forward and backward propagating in the cavity. In each figure, the upper limit of the ordinate is the unsaturated net model gain ($\Gamma_{xy} g_{th}$ - α_i), whereas the lower limit is the unsaturated total absorption (-($\Gamma_{xy}\alpha_{\mathrm{SA}}$ + α_i)).

Two features can be observed. First, due to the finite recovery rate, gain and absorption dynamics are strongly influenced by the coupling between the forward and the backward propagating pulses. An evidence of this statement is that at the point where E_f is almost the same for all the devices, forward $G(z)$ (Fig. 3.15b) is not identical but lower for device with higher E_b. Furthermore, although the local absorption bleaching seems stronger than the local gain compression, the integrations of these two quantities over the entire SA/gain section are equal, guaranteeing unitary round trip gain.

The latter feature also indicates that when a pulse circulating in the cavity, the pulse shortening in the SA compensates the pulse broadening in the gain section so that, in successive round trip, the pulse width remain constant. However if comparing different devices, we can find that device E which has the highest E_f and E_b in the SA and consequently highest absorption saturation, experiences strongest pulse shaping processes and therefore achieves the shortest pulse.

In conclusion, simulation results show that the device with longer SA exhibits higher intra-SA PE, resulting into stronger absorption saturation and shorter pulse. In addition, this result puts in evidence that larger intra-cavity pulse reshaping occurs in the device with longer SA, explaining the experimental findings in [97] that such device has worse noise performance and larger RF linewidth .

B. Change of L and R_L

Based on above observations, it is natural to expect further reduction of the pulse width in longer ML lasers since they have potential to incorporate even longer SA. Therefore, keeping the same L_{SA}/L (1:3.75) as device D, we considered two additional devices with total length of 3 and 5 mm whose corresponding R_L are 10.4% and 2.2%.

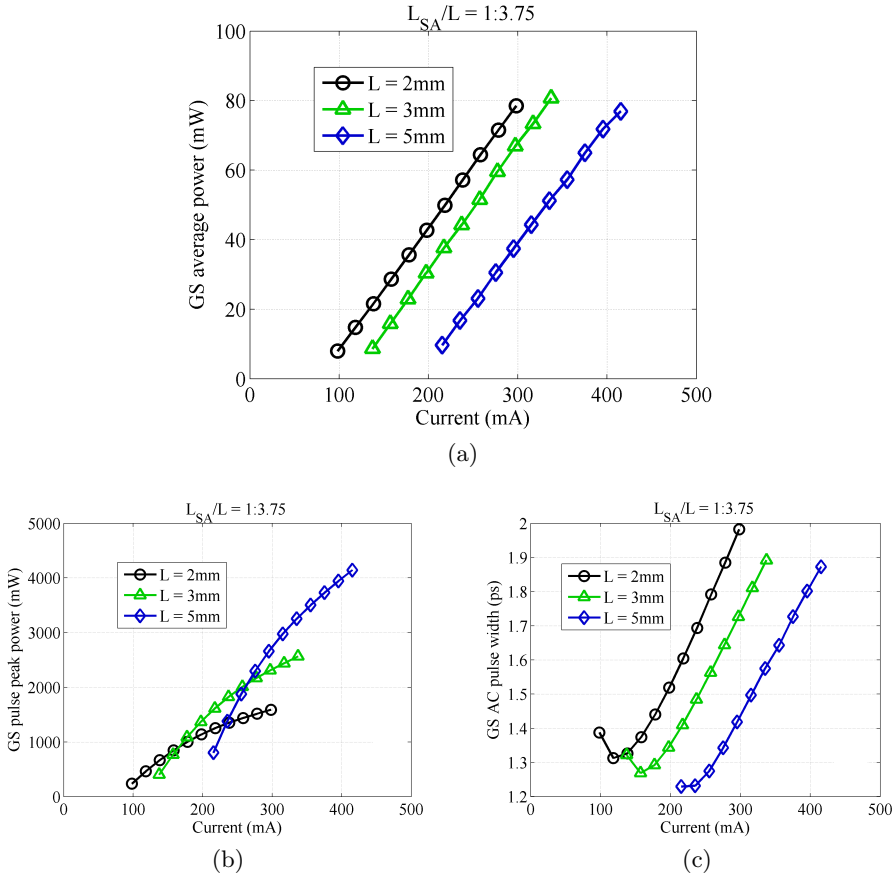

Figure 3.16: Three devices are considered with total length of 2 (circle), 3 (upward-pointing triangle) and 5 mm (diamond). As in Fig. 3.14, pulse performances of the average power (a), the peak power (b) and the AC pulse width (c) as a function of the injection current are reported.

Similarly as in Figs. 3.14 and 3.15, Figs. 3.16 and 3.17 report the pulse performances and the intracavity distributions of the pulse energy and of the modal gain for the three devices. We can see that for the device with the same L_{SA}/L, and at the same I_{eff}, similar average power and pulse width are achieved, leading to significant enhancement of the output peak power in longer devices (Figs. 3.16a, 3.16b and 3.16c).

Different from our expectation, the 5 mm device which has larger absolute SA length, it does not achieve big improvement in the pulse width with respect to its counterparts with the same L_{SA}/L. This observation can be explained as follows. First, the self-consistent ML pulse for the 5 mm device exhibits a larger E_b but a smaller E_f (Fig. 3.17a). As a result, this pulse leads to higher absorption saturation when it backward crosses the SA, while lower saturation in the forward path (Figs. 3.17b and 3.17c). Thus, the total pulse shortening effect experienced by this pulse actually is

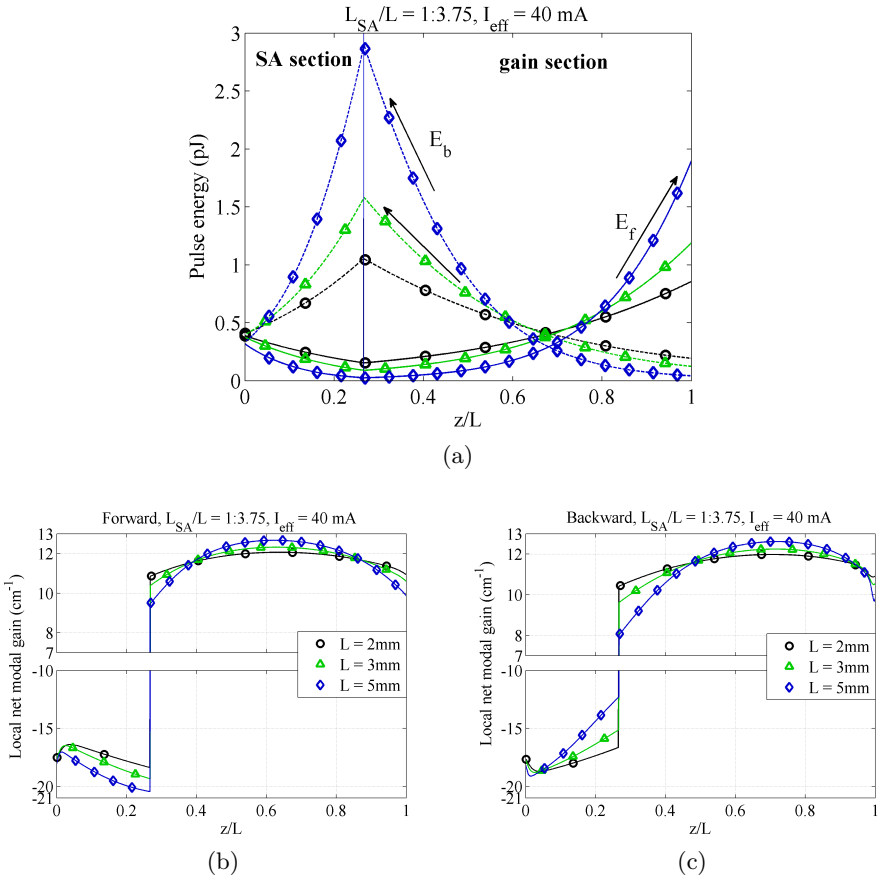

Figure 3.17: Three devices are considered with total length of 2 (circle), 3 (upward-pointing triangle) and 5 mm (diamond). The intracavity distributions of the PE (a) and of the forward (b) and backward (c) local net modal gain are shown.

similar to that in shorter devices. Another reason is that, since L_{SA}/L is fixed, the relative relation between the pulse shortening in the SA and the pulse broadening in the gain section is also fixed in each device, resulting therefore to similar total pulse shaping profile.

Previous results actually indicate that it is the length ratio L_{SA}/L not the absolute SA length who governs the achieved pulse width. In addition, to get shorter pulse, higher intra-SA PE and higher absorption saturation in both propagation directions are needed. We have to stress that although higher peak power can be achieved, further increase of the device total length may finally lead to early onset of the harmonic ML at high injection current [92].

C. Exchange of R_0 and R_L

All above devices belong to a main class of passively ML lasers, where the self-colliding pulse mode locking (SCPML) effect is utilized [69], i.e., the SA is close to the high-reflection coated facet (high R_0, see Fig. 3.12a). In this case, the pulse interacts with itself in the SA and enhances the absorption saturation. Recently it has been investigated in [98] a cavity configuration called anti-colliding pulse mode locking (ACPML) where on the contrary the SA is placed close to the low-reflection coated facet (low R_0, see Fig. 3.12b). Using this configuration, a even higher optical energy for pulse impinging the SA has been demonstrated theoretically in the QW devices. Therefore, according to our previous observation this configuration can be considered as another method to further reduce the pulse width.

Keeping $L = 5$ mm, we considered three high R_0 devices with L_{SA}/L of 1:4.3, 1:3.75 (the one discussed in Part B) and 1:2.9, the corresponding output reflectivities R_L are 0.7%, 2.2% and 33% (R_0 is always 95%). While for the low R_0 devices, we just exchanged the values between R_L and R_0.

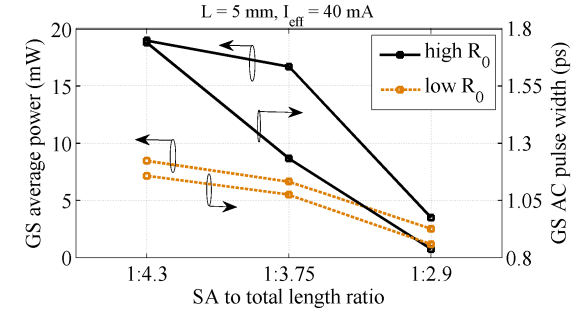

(a)

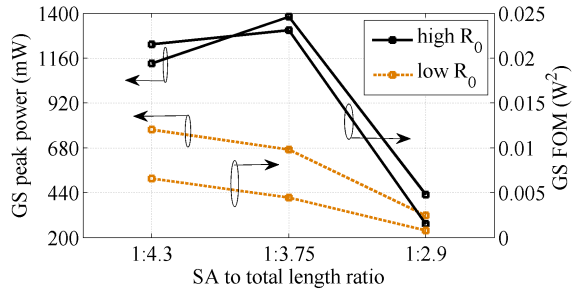

(b)

Figure 3.18: The average power and the AC pulse width (a), the peak power and the FOM (d) are shown as a function of the absorber-to-total length ratio at fixed I_{eff} for devices with high R_0 (black lines) and low R_0 (brown lines).

Figure 3.18 reports the pulse performances of these devices. We can observe similar trends in the low R_0 devices as that presented in Part A:

with increasing L_{SA}/L, a reduction in both the average power and the pulse width can be found, resulting to corresponding changes in the peak power and the FOM.

Comparing these two configurations, in [98], a substantial increase in the output peak power and a reduction in the pulse width have been demonstrated for device with low R_0. In our case however, big performance differences are found only in small L_{SA}/L devices and this differences vanish with increasing L_{SA}/L. In addition, although smaller pulse width is achieved in some cases of low R_0, the average power and peak power are always smaller.

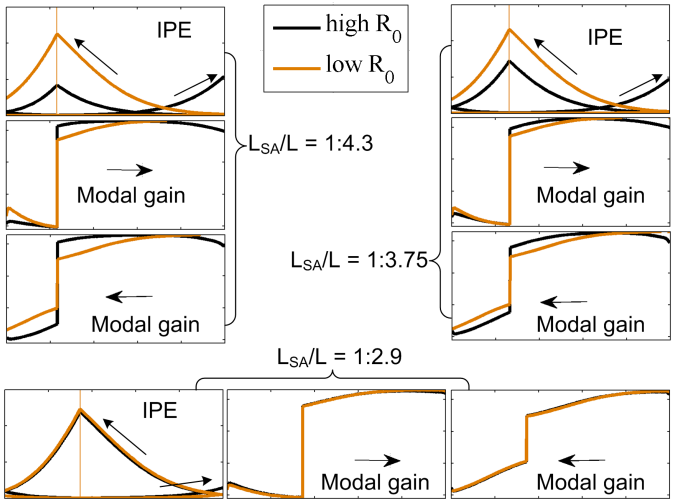

Figure 3.19: The intracavity pulse energy distribution, the forward/backward local modal gain for the devices shown in Fig. 3.18 which have high R_0 (black lines) or low R_0 (brown lines), and have different absorber-to-total length ratios of 1:4.3 (left), 1:3.75 (right) or 1:2.9 (bottom).

In order to identify the physical origin for the described performance differences, we show in Fig. 3.19 the intracavity PE evolution and the forward/backward local net modal gain distribution for these devices. This kind of figures has already been shown many times in previous parts, so here only schematics of them are reported.

When L_{SA}/L = 1:4.3 (left of Fig. 3.19), pulse in the low R_0 device experiences continuous amplification when propagating in the gain section without high power loss at the gain side facet that occurs in the high R_0 device, leading therefore to higher cumulated E_b before arriving the SA (z = L_{SA}). In this condition, the enhanced pulse energy in the SA strongly depletes the absorption in both forward and backward directions and consequently results to shorter pulses than that in the high R_0 device. On the contrary, although higher E_b impinging the SA is achieved in the low R_0 device, the pulse energy at the output facet for this device ($E_b(0)$) is lower than that for the high R_0 device ($E_f(L)$). Thus, the output average power

is lower. And since the pulse width reduction is not high enough, the output peak power is also lower. Instead, for the QW devices considered in [98], significant increase in the output peak power has been shown in the devices exploiting ACPML. We believe this difference can be attributed to the big difference in the SA length ratio between the QW and the QD devices, as explained below.

From Fig. 3.19, we can see that, with increasing L_{SA}/L, the intracavity PE profiles in these two kind of devices become similar or practically identical. The same phenomenon also happens in the corresponding intracavity local gain distributions. According to our previous findings, the device which has higher intra-SA PE will obtain shorter pulses. Therefore, the observations in Fig. 3.19 indicate that large difference in the pulse width should be found in two devices with very small L_{SA}/L. For the QW devices in [98], stable ML can be established in device with L_{SA}/L of only 2%, even if we take into account the difference between the maximum modal gain (g_0 = 120 cm^{-1}) and the unsaturated absorption (α_{SA} = 360 cm^{-1}) in that numerical model, the equivalent L_{SA}/L is still only 6%. Whereas, for the QD device in our model, $g_0 = \alpha_{SA}$ and the smallest L_{SA}/L is about 23%. Obviously, substantial reduction in the pulse width when using the ACPML configuration should be achieved in the QW case which also helps to obtain peak power enhancement in that case.

Therefore, previous discussions actually indicate that only for the QD device with smaller L_{SA}/L, this ACPML configuration is an efficient method to reduce the pulse width.

In this section, we present a systematic investigation of the device performances when varying the SA length, the total length and the cavity reflectivities. Throughout this investigation, we kept as constant the threshold modal gain and the reverse bias voltage, to ensure that all the devices have the same operation condition in terms of the gain and absorption saturation energies.

The obtained results reveal strong correlation between the intracavity pulse energy distribution and the ML performances. In detail, it is demonstrated that at the same effective pumping current, the higher the intra-SA pulse energy, the shorter the pulses. Especially, we show that if fixing the absorber-to-total length ratio, devices with longer total lengths exhibit similar pulse width and average power, but significantly enhanced peak power.

3.5 Dual-state ML regime

During the development of the monolithic passively mode locked QD lasers [11], [99], [96], various lasing regimes, and in particular ML operating regimes have been observed experimentally [100], [101], [102], such as the sole ground state ML, the most recently investigated sole excited state ML

[103] (by our collogues Breuer *et al.* from University of Athens (Greece)) and the dual-state (GS and ES) ML [104](by our collogues Cataluna *et al.* from University of Dundee (UK)). The last two ML regimes were found always in the devices with active region consisting of few stacked layers of self-assembled QDs, since ES gain is still well below threshold when GS lasing turns on in devices with 10 or 15 QD layers. Therefore in this analysis we consider devices with only 5 InAs/InGaAs QD layers.

Unlike the generally observed GS ML which has already been comprehensively studied [11], detailed theoretical investigations of the dual-state ML regime are still not presented so far. A full understanding of the complex dynamics happening in the gain and the SA sections has been found to be essential in explaining this novel-operating regime. Recently, reverse-emission-state-transition and the two-state ML regime in a strongly chirped QD laser under very low reverse bias voltage of the SA (0 V to -1 V) were demonstrated experimentally and theoretically in [103]. Instead of the large time TDTW model used in [103], a more efficient numerical model is exploited in this work, enabling a more detailed and wider investigation of the dual-state ML regime in QD two-section ML lasers.

In Subsection 2.5, we have presented a modified version of the MS-DDE model proposed in [58]. This model can be used for the dual-state ML simulation, which guarantees sufficient accuracy and high computational efficiency at the same time. In order to clarify the correctness of this revised MS-DDE model used in this work, the model has been first used to simulate the two-section ML laser with highly chirped QD active region in [103], very similar dynamic regimes and pulse performances were observed with approximately a 20-fold decrease in the simulation time. Furthermore, successful simulations were also done with FDTW to verify some cases examined in this paper. Therefore, although this MS-DDE model is not as rigorous as the complex TDTW model, we believe the main mechanisms in a QD two-section laser with dual-state lasing are properly considered in it. Consequently, an extensive analysis of the dependence of ML regimes on the device cavity and bias parameters can be efficiently preformed with this revised MS-DDE model.

In Subsection 3.5.1, the static and dynamic behaviours of the gain and absorption at GS and ES wavelengths are reported. These results clearly show that some commonly observed advantages of QD active medium, which are also the key factors to obtain stable and high quality ML from the QD GS, are weakened to a certain extent for ES ML. In addition, we found that, for two-section lasers, the GS pulse-induced gain and absorption changes tend to prevent partially the possibility of lasing from higher energy states (ES in this work). The ES pulse-induced gain and absorption variations on the contrary favor the onset of GS lasing. Both effects are more pronounced at low injection current and low SA voltage. These physical considerations allow to give a clear interpretation of the device performances discussed in

the following subsections.

In Subsection 3.5.2, the simulation results of the lasing and ML operating regimes of two passively ML lasers with different intrinsic cavity losses are shown and discussed. In particular, we show that, at relatively low reverse bias voltages and low gain currents, unstable dual-state ML with slow amplitude modulation of the pulse amplitude is obtained, as found experimentally in [103], [104]. On the contrary, when we increase both the voltage and the current, a stable dual-state ML is achieved which, to best of our knowledge, has not been reported in literatures yet. Especially, in the latter case, simultaneous GS and ES MLs are achieved with the same repetition rate for both states, and with significantly enhanced pulse peak power and pulse width.

In Subsection 3.5.3, we explained the difficulties to get sole ES ML with respect to the typically observed sole GS ML, based on the information presented in Subsection 3.5.1.

3.5.1 Gain and absorption dynamics

The model parameters used in the rate-equation system for computing interband and intraband carrier transitions, are reported in Table 3.3. We consider a device with active region consisting of 5 InAs/$In_{.15}Ga_{.85}As$ DWELL layers and emitting around 1.3/1.18 μm from GS/ES. In this subsection, both the steady-state and the dynamic properties of the gain and the absorption for GS and ES are studied, under different bias and excitation conditions. This preliminary analysis will be essential for discussing and understanding the significant differences between GS and ES lasing and ML regimes achieved in the two-section QD ML lasers studied in Subsection 3.5.2.

Steady state behaviors

Fig. 3.20a shows the steady state evolution of the material gain from the GS (g_{GS}) and ES (g_{ES}) transitions as a function of the injection current density J. These results are calculated by searching for the steady state solution of the rate-equation system under different J, when assuming no optical field is present (so without optical power-induced gain/absorption depletion). The same parameters are depicted also in Fig. 3.20b but as a function of the corresponding averaged carrier density n in the entire DWELL layers (divide the total carrier number in the quantum well and QD states by the volume of DWELL layers).

The behaviors of the corresponding differential gains dg_k/dn (k = GS, ES) are also shown in Fig. 3.20b. For semiconductor devices, the rate of change of the gain with the total carrier density dg_k/dn generally decreases when n increases due to the limited density of available states. Consequently,

Table 3.3: Dual-state mode-locked laser: main model parameters used in the rate equation system

Symbol	Description	Values
H_W	QW width	5 nm
$v_{g,GS}$	GS group velocity	$8.967 \cdot 10^7$ m/s
$v_{g,ES}$	ES group velocity	$8.772 \cdot 10^7$ m/s
N_{lay}	number of QD layers	5
N_d	QD surface density	$2.7 \cdot 10^{10}$ cm^2
$2\hbar\Gamma$	gain spectral bandwidth	34 meV
Γ_{xy}	field confinement factor	5.24%
$g_{0,k}$	material gain coefficient k = ES, GS	379.4, 227.6 cm^{-1}
$\tau_{SCH \to QW}$	relaxation time from SCH to QW	24.2 ps
$\tau_{QW \to ES_2}$	relaxation time from QW to ES_2	0.3 ps
$\tau_{ES_2 \to ES_1}$	relaxation time from ES_2 to ES	0.2 ps
$\tau_{ES_1 \to GS}$	relaxation time from ES to GS	0.2 ps
$\tau_{Aug,k}$	Auger recombination times from k = ES_2, ES, GS	110, 275, 660 ps
$\tau_{sp,k}$	spontaneous emission recombination times from k = ES_2, ES, GS	2, 2.7, 2.7 ns
$\tau_{nr,k}$	interband recombination times from k = SCH, WL	400, 400 ps
$\hbar\omega_k$	interband transition energies for k = ES_2, ES, GS	1.114, 1.054, 0.9879 eV
V_{bi}	built-in potential of the p-i-n junction	-0.8 V

the material gain will remain almost constant in a wide range of high injection current density. This well-known gain saturation effect is achieved at much lower pumping current density in QD device with respect to its bulk and quantum well counterparts due to the reduced density of states. As expected from above considerations, early GS gain saturation at moderate pumping level is observed in Fig. 3.20a. In addition, a much higher GS differential loss $d\alpha_{GS}/dn$ in the absorption regime (when $g_{GS} < 0$ cm^{-1}) with respect to the differential gain dg_{GS}/dn in the gain regime (when $g_{GS} > 0$ cm^{-1}) is highlighted in Fig. 3.20b. However, it is also clearly shown that these properties are weakened for the ES, where the material gain, although

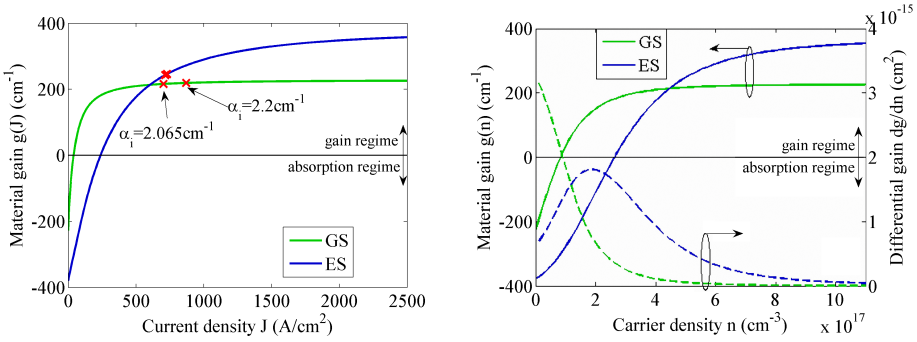

Figure 3.20: (a) The steady state behaviour of QD material gain from GS (green) and ES (blue) transitions as a function of the injection current density J. The red-cross markers represent the corresponding GS and ES threshold gain when intrinsic losses equal to 2.065 cm^{-1} and 2.2 cm^{-1} respectively, which will be discussed later on in Fig. 3.22. The horizontal black line, located at gain equals to 0 cm^{-1}, distinguish the gain and absorption regimes of the active medium; (b) The steady state behaviour of material gain (solid line) and differential gain (dashed line) from GS (green) and ES (blue) transitions as a function of the averaged carrier density n in the DWELL layers.

much higher, has a significantly reduced $d\alpha_{ES}/dn$ and a higher dg_{ES}/dn at the usual operating current density level.

This big difference between GS and ES differential gains/losses has an important influence on the achievement of stable ML pulses from these two transitions in the passively mode locked lasers.

As discussed in Section 3.1, the well-known S parameter has been verified to play an important role in determining the performances of the ML systems [95]. For ML operation, the increase of this parameter will benefit the ML stability as well as the obtained pulse quality [95]. Using Eq. (3.3) and referring to Fig. 3.20a, we predict that GS ML could be established more easily and with an improved stability respect to ES ML, since S_{GS} is always much larger than S_{ES}.

Transient responses to external optical excitations

To complete the preliminary analysis, the transient responses of a gain section, acting as a semiconductor optical amplifier, and a reverse biased SA to an externally injected optical pulse are studied using the approaches described in [74]. Been Γ_{xy} the field confinement factor, in this work we will indicate with $\Gamma_{xy}\Delta g_{m\leftarrow n}$ the time-dependent modal gain compression from m = GS, ES caused by a pump pulse resonant with the n = GS, ES transition. Similarly, the time-dependent modal absorption bleaching will be $\Gamma_{xy}\Delta\alpha_{m\leftarrow n}$.

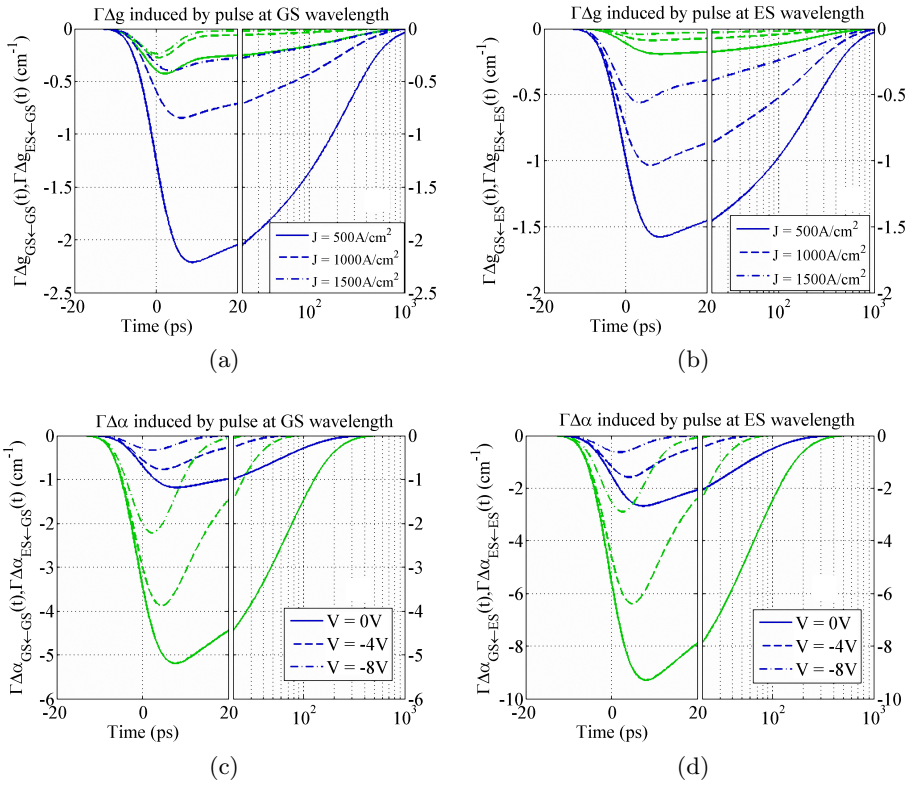

Figure 3.21: (a) The temporal evolution of GS (green) and ES (blue) modal gain compressions induced by a Gaussian pulse with 1 pJ energy, 10 ps duration, resonant with GS transition and traveling in a SOA biased with current density of 500 A/cm^2 (solid line), 1000 A/cm^2 (dashed line), and 1500 A/cm^2 (dot-dash line). Time interval -20 ps $<$ t $<$ 20 ps is shown in the linear scale, whereas time interval 20 ps $<$ t $<$ 1000 ps is shown in the logarithmic scale; (b) Same quantities as in (a) induced by a Gaussian pulse with the same properties but resonant with ES transition; (c) The temporal evolution of the absorption bleaching induced by a Gaussian pulse resonant with GS transition and traveling in a SA with 0V (solid line), -4V (dashed line) and -8V (dotted line) reverse bias; (d) As in (c) but for a Gaussian pulse resonant with ES transition.

In Fig. 3.21a and Fig. 3.21c, we report respectively the temporal evolutions of the modal gain compression ($\Gamma_{xy}\Delta g_{GS\leftarrow GS}$, $\Gamma_{xy}\Delta g_{ES\leftarrow GS}$) and the modal absorption bleaching ($\Gamma_{xy}\Delta\alpha_{GS\leftarrow GS}$, $\Gamma_{xy}\Delta\alpha_{ES\leftarrow GS}$), induced by a Gaussian pulse with 1 pJ energy, 10 ps duration (typical value for QD ML pulses) and resonant with the GS transition. On the contrary, the dynamics of the same quantities induced by a pulse with the same properties, but resonant with the ES transition ($\Gamma_{xy}\Delta g_{GS\leftarrow ES}$, $\Gamma_{xy}\Delta g_{ES\leftarrow ES}$, $\Gamma_{xy}\Delta\alpha_{GS\leftarrow ES}$ and $\Gamma_{xy}\Delta\alpha_{ES\leftarrow ES}$) are shown in Fig. 3.21b and Fig. 3.21d respectively. The considered SOA/SA waveguide has a 6 μm ridge width and a short

total length to avoid the influence of field propagation effects.

Increasing J from 500 to 1500 A/cm^2, a significant decrease in the entire gain recovery time (from ns scale to approximately tens ps) and in the maximum gain compression ($\Gamma_{xy}\Delta g_{GS\leftarrow GS}$ and $\Gamma_{xy}\Delta g_{ES\leftarrow ES}$) for both states is observed (Fig. 3.21a and Fig. 3.21b) due to the enhanced carrier relaxation from higher electrical pumping levels. In addition, ES gain compression is found always to be much larger than that of the GS when excited by a pulse with the same energy, which means the GS amplification is harder to saturate than the ES amplification.

Similarly, increasing reverse bias voltage from 0 to -8 V, a significant reduction in the absorption recovery time (from hundreds to few ps) and in the maximum absorption bleaching ($\Gamma_{xy}\Delta\alpha_{GS\leftarrow GS}$ and $\Gamma_{xy}\Delta\alpha_{ES\leftarrow ES}$) for both states is also observed (Fig. 3.21c and Fig. 3.21d), due to the enhanced thermionic and tunneling carrier escape mechanisms in the SA [45]. Additionally, if biased with the same voltage, the absorber always shows larger absorption depletion in GS transition than in ES transition, which means ES absorption is harder to saturate if compared with GS absorption.

The dynamic properties described above confirm again that GS ML can be achieved more easily, since it is easier to obtain simultaneous pulse shortening and amplification mechanisms from GS transition.

The photon-generated carriers at ES are quickly swept out during the pump pulse (10 ps), leading to smaller absorption bleaching in ES. There are two main aspects responsible for this fast carrier sweep-out. One is the smaller intraband energy difference between ES and the separate confinement heterostructure level, thus carriers at ES are swept out faster via the tunneling escape. Another one, which is more important, is the extremely fast carrier relaxation from ES to the GS (hundreds fs), existing as an additional carrier sweep-out path. The latter aspect is referred to as the photon-pumping process in [37]. This process and the related fast carrier escape (about 1 ps) from GS to ES guarantee the recovery of a quasi-equilibrium distribution in the QD layers and are responsible for the associated transient changes in GS/ES induced by a pulse resonant with ES/GS. These dynamics imply the strong coupling between GS and ES gain/absorption saturations and are key effects in determining the lasing regimes.

For a typical single section laser, the modal gain is clamped at its threshold value when lasing is achieved. For the two-section passively ML laser, however, the absorption bleaching in the SA induced by the non-zero optical power after lasing onset, allows the device to operate at a modal gain which is even smaller than its threshold value. For example, if we assume the threshold current for ES lasing $I_{th,ES}$ is larger than that for GS $I_{th,GS}$, GS lasing is achieved first. When changing the bias condition, this lasing can be sustained, if the photon-induced absorption bleaching $\Gamma_{xy}\Delta\alpha_k$ and gain compression $\Gamma_{xy}\Delta g_k$ (k = GS in this case) balance the following equation:

$$\frac{L_{\text{gain}}}{L}\left(\Gamma_{xy}g_{k,th}+\Gamma_{xy}\Delta g_k\right)-\frac{L_{\text{SA}}}{L}\left(\Gamma_{xy}\alpha_{k,th}+\Gamma_{xy}\Delta\alpha_k\right) - \alpha_i-\frac{1}{L}\ln\left(\frac{1}{\sqrt{R_0R_L}}\right)=0 \tag{3.12}$$

where $\Gamma_{xy}g_{k,th}$ is the modal gain at the threshold current for the first lasing state (in this case the GS), $\Gamma_{xy}\alpha_{k,th}$ is the modal loss at the same current, L_{gain} is the length of the gain section, L_{SA} is the length of the SA, L is the total device length which equals to $L_{\text{gain}} + L_{\text{SA}}$, α_i is the cavity intrinsic losses, and R_0 and R_L are the reflectivities at the SA and the gain section side facets respectively. One should note that, unlike the transient response $\Gamma_{xy}\Delta g_{m\leftarrow n}$, $\Gamma_{xy}\Delta g_k$ in Eq. (3.12) represents the modal gain changes at k = GS, ES transition induced by the optical power (from both GS and ES) in the cavity, and averaged over time and the length of the gain section. Similarly, $\Gamma_{xy}\Delta\alpha_k$ is the modal absorption changes averaged over time and the length of SA.

Obviously, ES round trip gain Eq. (3.12) is negative at GS threshold current $I_{th,GS}$. However, at higher current, if the GS photon-induced gain/absorption changes in the ES satisfy the condition

$$|\Gamma_{xy}\Delta g_k| < (L_{\text{SA}}/L_{\text{gain}})\,|\Gamma_{xy}\Delta\alpha_k| \tag{3.13}$$

there will be a positive change in the original ES overall round trip gain and therefore the onset of lasing from ES is facilitated. On the contrary, if the condition

$$|\Gamma_{xy}\Delta g_k| > (L_{\text{SA}}/L_{\text{gain}})\,|\Gamma_{xy}\Delta\alpha_k| \tag{3.14}$$

holds, there will be a negative change in the round trip gain and therefore ES lasing will tend to be inhibited. Situations are the same if inversely ES lasing happens first.

From the above discussions and from Fig. 3.21a and Fig. 3.21c, we find that if lasing from GS is achieved first, GS optical field will lead to similar level of changes in ES gain, $\Gamma_{xy}\Delta g_{ES\leftarrow GS}$ = -0.4 $\sim$ -2.2 cm^{-1} and absorption, $\Gamma_{xy}\Delta\alpha_{ES\leftarrow GS}$ = -0.3 $\sim$ -1.2 cm^{-1}. ES lasing is therefore inhibited at certain bias conditions (satisfying Eq. (3.14), since L_{SA} is generally much shorter than L_{gain} for QD passively ML laser ($L_{\text{SA}}/L_{\text{gain}} = 0.1 \sim 0.25$).

On the contrary, if lasing from ES is achieved first, thanks to the very efficient photon-pumping process, the generated ES carriers quickly relax towards the GS, contributing to the large absorption saturation at the GS wavelength. Thus, appreciable reduction of GS saturable losses Γ_{xy}

$\Delta\alpha_{GS\leftarrow ES}$ = -3 $\sim$ -9 cm^{-1} with respect to the tiny small reduction of GS gain $\Gamma_{xy}\Delta g_{GS\leftarrow ES}$ = -0.04 $\sim$ -0.2 cm^{-1} (Fig. 3.21b and Fig. 3.21d) are observed, and lasing from GS is promoted (satisfying Eq. (3.13)). Therefore, we can conclude that lasing from GS tends to be achieved much more easily with respect to the lasing from ES in the two-section QD lasers. Note that these effects are more evident at low current and low SA voltage.

In the following subsections, we show how the investigated static and dynamic properties of the gain and the absorption influence the achieved lasing and ML regimes in the InAs/InGaAs QD based devices.

3.5.2 Sole GS ML and dual-state ML

We consider in this subsection two ridge-waveguide edge-emitting QD ML lasers with different intrinsic losses α_i of 2.065 cm^{-1} and 2.2 cm^{-1} to change the laser operation point on the gain characteristic curves. Both devices have a fixed total length of 2 mm, absorber length L_{SA} of 300 μm, ridge width of 6 μm, high reflection coating at the SA side facet with $R_{0,k} = 99\%$ (k = ES, GS) and low reflection coating at the output facet with $R_{L,k} = 10\%$. The parameters of the active medium are those considered in Subsection 3.5.1.

Lasing regime discussion

For these two devices, in Figs. 3.22a and 3.22b respectively, maps of the achieved operating regimes are reported in the injection current and reverse bias voltage plane, summarizing the corresponding lasing state at each bias point. In addition, in Fig. 3.20a, the associated threshold material gains for the lasing from GS ($g_{th,GS}$) and ES ($g_{th,ES}$) transitions of the same devices are shown as red-cross markers on the corresponding gain curves. The threshold material gain can be computed following Eq. (3.12) by setting $\Gamma_{xy}\Delta g_k$ and $\Gamma_{xy}\Delta\alpha_k$ to zero.

With increasing current, g_{GS} shows earlier saturation than g_{ES}, therefore a slight increase in the intrinsic losses leads to a large increase in the GS threshold current $I_{th,GS}$, whereas for the ES, threshold current $I_{th,ES}$ does not show severe increase due to the larger dg/dJ. More precisely, the computed results show that $I_{th,GS} < I_{th,ES}$ when α_i = 2.065 cm^{-1} and $I_{th,GS} > I_{th,ES}$ when α_i = 2.2 cm^{-1} (Fig. 2a).

The relative relationships between $I_{th,GS}$ and $I_{th,ES}$ are the key reasons governing the achieved lasing regimes in Figs. 3.22a and 3.22b. Furthermore, in order to get more insight on the physical origin of the different lasing regimes, the time-space-averaged occupation probabilities ρ in SA and gain sections of GS and ES at several fixed reverse voltages are depicted in Fig. 3.23a-3.23d as a function of the injection current.

For the first device (Fig. 3.22a), $I_{th,GS}$ is slightly smaller than $I_{th,ES}$,

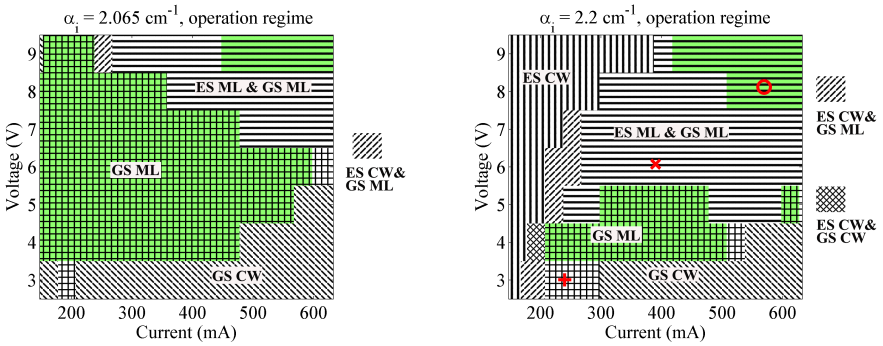

Figure 3.22: Maps of the operation regime as a function of the injection current for the gain section and the reverse bias voltage applied to the SA for QD two-section ML laser with intrinsic losses of 2.065 cm^{-1} (a), and 2.2 cm^{-1} (b). There are two layers in each figure; the background layer distinguish the bias condition region that achieves stable ML regime with green color; the top layer indicates various operation regimes by filling the corresponding bias condition region with different line styles: GS continuous wave (GS CW, forward diagonal line), ES continuous wave (ES CW, vertical line), simultaneous GS and ES continuous wave (ES CW & GS CW, diagonal cross), GS mode locking and ES continuous wave (ES CW & GS ML, backward diagonal line), sole GS mode locking (GS ML, large grid), simultaneous GS mode locking and ES mode locking (ES ML & GS ML, horizontal line). Cross, circle and plus markers in (b) identify the operation points which will be discussed later.

therefore GS lasing is achieved first; the self-consistent solution of the DDE equations and rate-equation system for GS is obtained in a large range of bias conditions above the first lasing threshold $I_{th,GS}$. The balance between the occupation probability changes in the SA $\Delta\rho_{\mathrm{SA}}$ and the gain section $\Delta\rho_{\mathrm{gain}}$ is observed when increasing current above the threshold, always satisfying Eq. (3.12). This can be verified by substituting in Eq. (3.12) the following equations: $\Gamma\Delta g = 2\Gamma g_0 * \Delta\rho_{\mathrm{gain}}$ and $\Gamma\Delta\alpha = -2\Gamma g_0 * \Delta\rho_{\mathrm{SA}}$, being g_0 the material gain coefficient. We can see from Fig. 3.23a and Fig. 3.23b that, $\Delta\rho_{\mathrm{SA}}$ and $\Delta\rho_{\mathrm{gain}}$ of GS always obey the rule that $|\Delta\rho_{\mathrm{gain}}| = |\Delta\rho_{\mathrm{SA}}| * L_{SA} / (L - L_{SA})$ (L_{SA} = 0.3 mm is the SA length, and L - L_{SA} = 1.7mm is the gain section length), preserving the lasing from GS. In addition, consistently with the information obtained in Subsection 3.5.1, due to the optical power from GS, lasing from ES is prevented, especially at low reverse bias voltage (-3 V and -6 V). As an evidence, there is a large reduction in ρ_{gain} but only a slight increase in ρ_{SA} for the ES, which satisfies the condition 3.14. By increasing the reverse voltage, due to the enhanced absorption recovery rate (Fig. 3.21c) and the reduced GS optical power, maximum GS absorption bleaching (Fig. 3.23a) decreases severely. To guarantee unitary round trip gain, the corresponding GS gain compression also decreases (Fig.

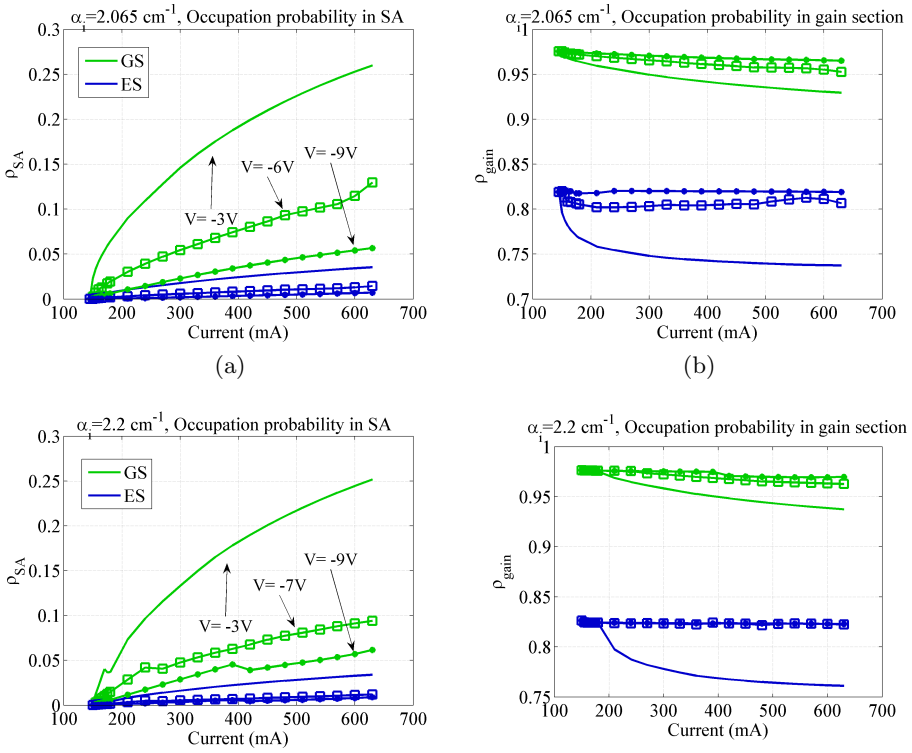

Figure 3.23: Time-space-averaged occupation probability in the SA (a) and gain section (c) of the GS (green) and ES (blue) for a QD ML laser with intrinsic losses of 2.065 cm^{-1} when SA reverse bias voltage is -3V (solid line), -6V (square marked) and -9V (star marked). Time-space-averaged occupation probability in the SA (b) and gain section (d) of the GS (green) and ES (blue) for a QD ML laser with intrinsic losses of 2.2 cm^{-1} when SA reverse bias voltage is -3V (solid line), -7V (square marked) and -9V (star marked).

3.23b), therefore the associated $\Delta\rho_{\text{gain}}$ of ES becomes negligible. Under this condition, if we increase also the injection current, GS pulse energy will increase, leading to larger ES absorption bleaching. At the same time, negligible ES gain compression is still guaranteed due to enhanced carrier pumping process at high current level. So finally, onset of ES lasing can be achieved when ES absorption bleaching is high enough to compensate the original negative total cavity gain of ES. Furthermore, increasing the reverse voltage, since the ES gain compression decreases, the needed reduction level of the ES absorption also decreases; consequently the onset current of ES lasing is shifted toward lower current.

The numerically obtained operation regimes in the first device is qualitatively consistent with the experimental observations in [104], where coexisting ES and GS lasing are achieved at high injection current and high

reverse bias voltage. In addition, the onset current of ES lasing is shown to decrease, though not monotonically, with increasing the reverse voltage.

On the contrary, for the second laser with $\alpha_i = 2.2$ cm^{-1} (Fig. 3.22b), $I_{th,ES}$ is now smaller than $I_{th,GS}$ (see Fig. 3.20a), ES lasing is therefore always achieved first. In this case, GS lasing can not be self-starting. However, as we mentioned in Subsection 3.5.1, optical power from ES will leads to severe reduction in the GS absorption (Fig. 3.23c) due to the fast relaxation of the photon-generated ES carriers towards the GS in the SA. Furthermore, a relatively smaller compression of GS gain (Fig. 3.23d) is obtained. These two changes easily satisfy Eq. (3.13) and therefore reduce GS round trip cavity losses; this effect becomes stronger at larger current since ES power becomes larger. Therefore, when the current is sufficiently high, GS lasing turns on. Additionally, increasing the reverse voltage, photon-generated carriers at ES are swept away more efficiently via the enhanced thermionic and tunneling escape processes. As a result, the amount of carriers that relax from ES to GS reduces significantly, leading to a reduction in the effectiveness of the ES induced positive compensation of GS total cavity losses. Consistently with this, in Fig. 3.22b, onset current of GS lasing is postponed to higher value when SA voltage increases.

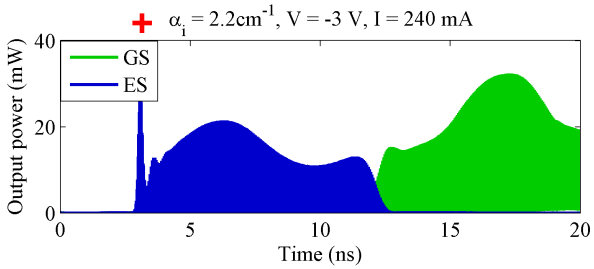

Figure 3.24: Time trace of the output peak power of GS (green) and ES (blue) at the initial 20 ns time interval of the simulation for the device shown in Fig. 3.22b when injection current is 240 mA and reverse voltage is -3 V (the plus marker in Fig. 3.22b).

Once the lasing from GS is achieved, the operation conditions will become similar to those of the first device. At lower voltage, see example in Fig. 3.24, ES emission starts first, leading to large GS absorption bleaching in the SA and favoring the lasing from GS. Once GS lasing starts, thanks to the already bleached SA absorption, GS lasing can be self-sustained even without the ES emission. In addition, ES lasing is prevented for the reasons described in Subsection 3.5.1 and previously for the first device. This can be validated by the large gain compression and relative small absorption bleaching of ES when V = -3 V (Fig. 3.23c and Fig. 3.23d), which is exactly the same situation that happens in the first device. Based on the same reason, at larger reverse voltage, dual-state lasing is obtained.

The simulated operation regimes for this device is instead shown to be in qualitatively agreement with the experimental results in [103], where reverse-emission-state-transition, i.e., ES lasing is achieved first and then followed by GS lasing at higher current, is observed. As we discussed here, the onset of GS lasing is shifted toward larger current when increasing the reverse voltage.

ML performances discussion

We take the device with $\alpha_i = 2.2$ cm^{-1} as an example for further investigations on the ML characteristics. The maps of peak power and pulse width of ML regimes from GS and ES are reported in Fig. 3.25a-3.25d in a plane of the forward injection current and the reverse bias voltage.

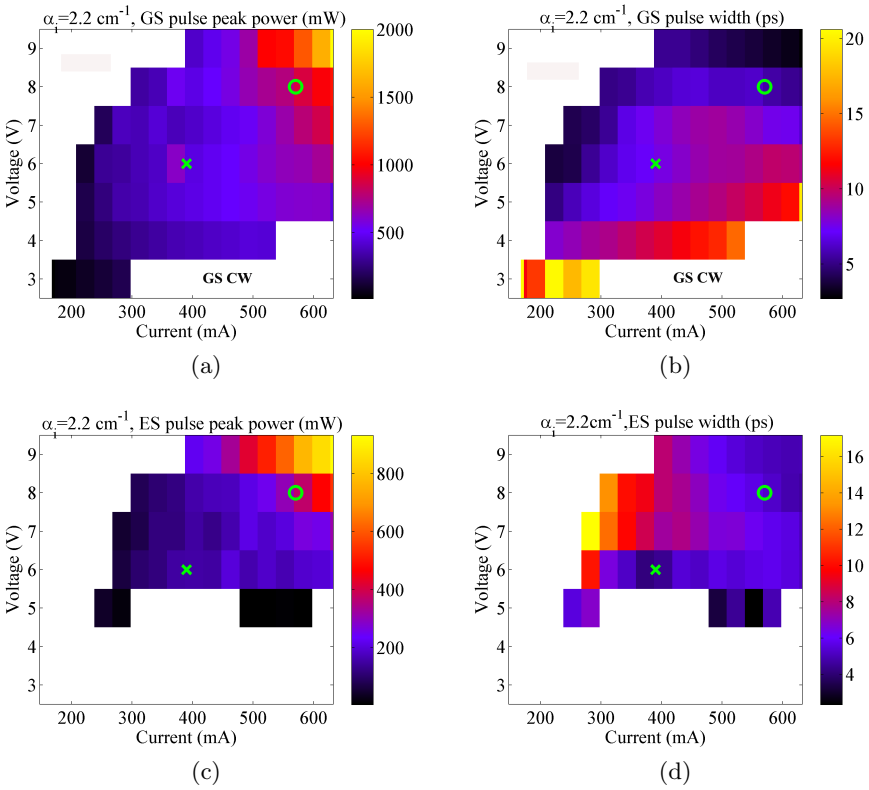

Figure 3.25: Maps of GS pulse peak power (a), ES pulse peak power (b), GS pulse width (c) and ES pulse width (d) as a function of the injection current and reverse voltage for the device with intrinsic losses is 2.2 cm^{-1} as shown in Fig. 3.22b.

From Fig. 3.22b, we can find that a variety of ML regimes are achieved in this device. It is noteworthy to point out that, although sole ES lasing is obtained in a large range of bias conditions, sole ES ML is never observed. The restrictions to achieve sole ES ML will be discussed in detail

in Subsection 3.5.3. Consistently with the commonly observed experimental performances for the typical GS ML QD lasers [11], the maximum GS peak power and the minimum GS pulse width are observed at low current and high voltage when sole GS ML is achieved (Fig. 3.25a and Fig. 3.25b). Just beyond the sole GS ML region, at higher current, the leading edge instability induced by spontaneous emission noise is encountered, which finally results in continuous wave operation of the GS.

On the contrary, within dual-state ML region, in most of the bias conditions, an unstable dual-state ML with regular amplitude modulation is observed (Fig. 3.22b), with similar pulse width and peak power as sole GS ML (Fig. 3.25a and Fig. 3.25b). Nevertheless, it is noticeable that at high current and high voltage, a stable dual-state ML regime is achieved, accompanied with remarkable enhanced pulse peak power and pulse width for both ES and GS. This stable ML regime can be obtained only in limited bias conditions, since at higher current (beyond the bias condition in Fig. 3.22) the LEI will start to appear first in the GS ML. Two operating conditions, one representing the unstable dual-state ML (the cross marker, V = -6 V, I = 390 mA) and another representing the stable dual-state ML (the circle marker, V= -8 V, I = 570 mA), are studied in detail later.

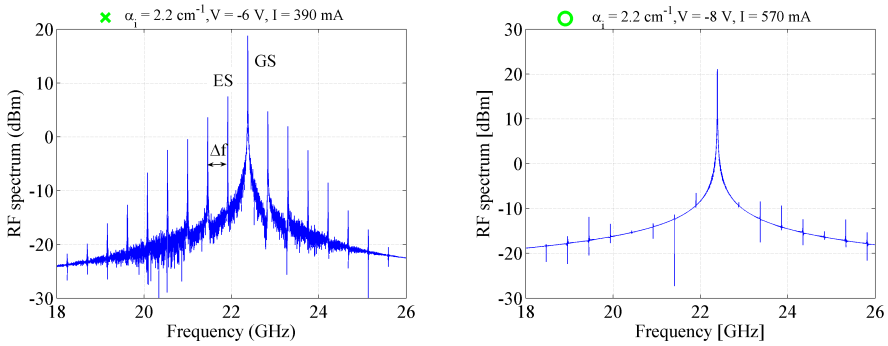

(a) (b)

Figure 3.26: For the device with intrinsic losses is 2.2 cm^{-1} as shown in Fig. 3.22b, the RF spectra of the pulse trains when the laser is biased with V = -6 V, I = 390 mA (a) and biased with V = -8 V, I = 570 mA (b), corresponding to the cross and circle markers shown in Fig. 3.25a - 3.25d respectively.

In Fig. 3.26a and Fig. 3.26b, the radio frequency spectra of these two conditions are reported in a narrow frequency window around the fundamental repetition frequency. For the first operating condition, two distinct fundamental lines appear in the RF spectrum (Fig. 3.26a), corresponding respectively to the pulse train of GS with a repetition frequency f_{GS} = 22.374 GHz and the pulse train of ES with a repetition frequency f_{ES} = 21.915 GHz. This difference in the repetition frequencies confirms the different group velocities of GS and ES pulses. As shown in Fig. 3.27, this

difference not only leads to desynchronization between GS and ES pulse trains, but also results in an amplitude modulation characterized by a periodicity of $1/\Delta f$ ($\Delta f = f_{GS}$ - f_{ES} = 459 MHz). In frequency domain, this is equivalent to multiple side-bands around the fundamental GS and ES lines with lower power and equal separation f between each other. This RF spectrum shows qualitative agreement with the experimental observations in [103], where both the fundamental lines and the side-bands are present when dual-state ML is achieved. On the contrary in [104], although dual-state ML is also observed, the achieved ES pulse power at the shown bias condition is very small with respect to the GS pulse power, extremely weakening the influence of the ES pulse on the GS pulse. As a consequence, the side-bands would have an even smaller power that is almost merged with the background noise. We believe this fact explains partially the absence of side lobes in the reported RF spectrum in [104]. We also observed that, in the simulations, the strength of this amplitude modulation and the side-band/main-peak power ratio change with the bias condition.

A completely different dynamic regime is instead found at the second operating point, where a single well defined line at f_{GS} is observed in the RF spectrum (Fig. 3.26b), indicating that the pulses from both states are propagating with the same velocity $v_{g,GS}$ ($v_{g,GS} > v_{g,ES}$) in the cavity. We find that this locked traveling of ES and GS pulses arises from the large forward shift of the ES pulse in time domain induced by the large positive net gain window preceding the pulse.

To clarify the physical origins of the amplitude modulation operation in the first condition and the locked pulse traveling in the second condition, the associated gain and absorption dynamics determining the generation of the mode locked pulses are depicted in Fig. 3.27 and Fig. 3.28. In these figures, the total losses $A(\tau)$ and the total amplification $G(\tau)$ experienced by the pulse during one complete round trip within the laser cavity are shown in detail.

Consistently with the presence of side-bands in the RF spectrum envelope, amplitude modulations are observed in the time domain pulse traces of GS and ES (Fig. 3.27a) with a characteristic periodicity $1/\Delta f$. Pulse evolutions and the associated $G(\tau)$ and $A(\tau)$ dynamics in two distinct short time intervals are zoomed in Fig. 3.27(c-d) and Fig. 3.27(e-g) respectively, corresponding to the highlighted region 1 and region 2 in Fig. 3.27a.

In the first time interval, ES pulse follows the GS pulse with a large relative delay. As discussed previously, GS lasing is always self-preserved and immediately leads to a significant reduction of the ES gain $G(\tau)$ (Fig. 3.27d). However, this GS pulse induced ES gain reduction now has enough time to recover back to a sufficient high value that overcomes the overall ES losses $A(\tau)$ before the arrival of the subsequent ES pulse. Therefore, ES pulse feels a positive net gain within one round trip and tends to be amplified. In addition, ES gain reduction induced by the ES pulse is compensated by

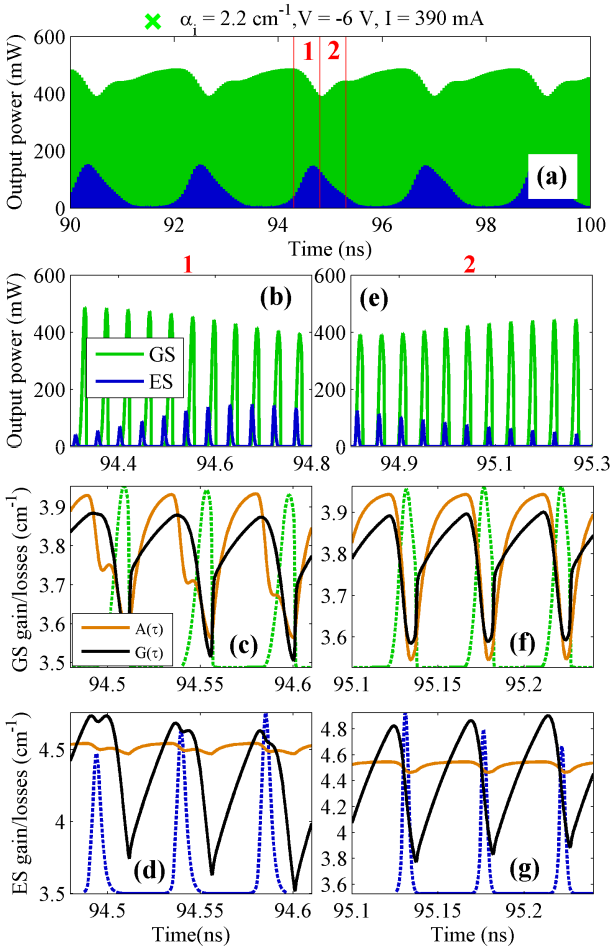

Figure 3.27: ML operation at V = -6 V, I = 390 mA, represented by cross marker in Fig. 3.25. (a) Time traces of the pulse output power from GS (green) and ES (blue) in a time interval from 90 ns to 100 ns. Output power from GS and ES (b), and the net gain window of GS (c) and ES (d) are shown in the zoomed time interval corresponding to the highlighted region 1 in (a). Output power from GS and ES (e), and the net gain window of GS (f) and ES (g) are shown in the zoomed time interval corresponding to the highlighted region 2 in (a). In the net gain window, the overall losses $A_{GS}(\tau)$ (brown line) and overall amplification $G_{GS}(\tau)$ (black line) experienced by the pulse during a single round trip in the cavity are shown with the corresponding pulse envelope (dashed line).

the carriers escaped from GS state, leading to an early started compression of the GS gain (Fig. 3.27c), which is encountered by the closely followed subsequent GS pulse, resulting in a gradual decrease in the GS pulse energy.

Due to the different group velocity, the relative delay between two adjacent GS and ES pulses increases with time in region 1 and finally ES pulse is overlapped with the followed GS pulse in the region 2 (Fig. 3.27e). In

this case, the GS pulse induces a large ES gain compression experienced by the synchronous ES pulse, as a result, ES pulse has a negative round trip gain and consequently its energy decreases gradually (Fig. 3.27g). On the contrary, the ES carriers produced by the absorption of ES pulse in the SA, quickly pump the lower energy GS, reducing significantly the GS absorption seen by the synchronous GS pulse. Due to this effect, positive round trip gain is achieved in GS, enhancing gradually GS pulse energy (Fig. 3.27f).

In [103], dual-stable ML is achieved at rather low reverse voltage (even at 0 V) and thus the interplays between GS and ES pulses are dominated by the absorption dynamics in the SA. Here, on the contrary the photon pumping process is much less efficient since device operate at very high reverse voltage and instead the coupled GS and ES gain dynamics in the gain section are instead dominating. This can be clarified by the fact that the increase or decrease of ES pulse energy is achieved at different relative time-location of ES and GS pulses with respect to that reported in [103].

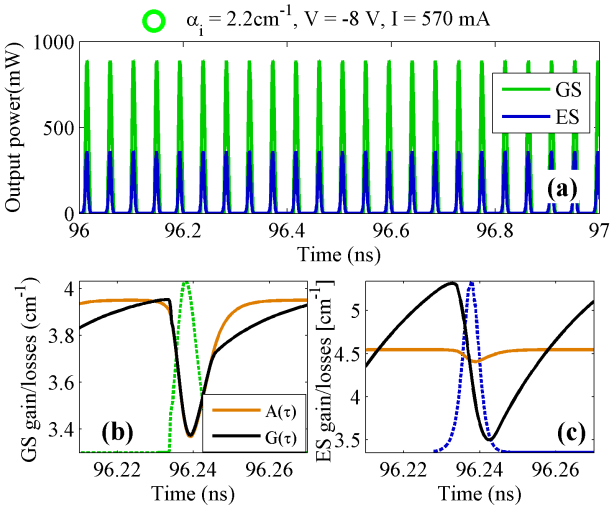

Figure 3.28: ML operation at V = -8 V, I = 570 mA, represented by circle marker in Fig. 3.25. (a) Time traces of the pulse output power from GS (green) and ES (blue) in a time interval from 96 ns to 97 ns. The net gain window of GS (b) and ES (c) are shown in the same zoomed time interval within the time interval in (a). In the net gain window, the overall losses $A_{GS}(\tau)$ (brown line) and overall amplification $G_{GS}(\tau)$ (black line) experienced by the pulse during a single round trip in the cavity are shown with the corresponding pulse envelope (dashed line).

For the second operating condition, well-formed pulse traces from GS and ES with negligible peak power jitter can be seen in Fig. 3.28a. The behavior of GS pulse can be easily understood by analyzing the evolutions of $G(\tau)$ and $A(\tau)$ in Fig. 3.28b. The overall round trip gain $G(\tau)$ equals exactly the overall losses $A(\tau)$ when there is the pulse, guaranteeing an identical reproduced pulse after one round trip. Being $G(\tau)$ smaller than $A(\tau)$ behind

the pulse, the noise perturbations following the pulse are eliminated, whereas the tiny positive net gain window before the pulse is not strong enough to lead to the LEI; therefore stable GS ML is sustained.

A very different ES net gain window with respect to that shown in Fig. 3.27 is observed in the second operating condition. In Fig. 3.28d and Fig. 3.28g, ES pulses leading edge and trailing edge experience simultaneous overall attenuation or amplification. Therefore, there is no relative shift of the pulse in time domain when circulating in the cavity and ES pulse travels with its own group velocity $v_{g,ES}$. In the second case, however, a positive/negative net gain window appears before/after ES pulse peak (Fig. 3.28c), contributing to an amplification of the leading edge optical field and an attenuation of the trailing edge optical field. Influenced by the combination of these two effects, ES pulse is forward shifted in the time domain, equivalent to say that it is propagating with a larger group velocity. Actually, this larger group velocity is equal exactly to $v_{g,GS}$ because, if a slight shift from $v_{g,GS}$ happens, the GS pulse induced gain and absorption changes will force the ES pulse to go back. Therefore, ES pulse seems to be clamped with the pulse from GS in this case.

This equal-group-velocity dual-state ML has not been reported in literatures so far. To further validate the results, a reduced set of simulations in similar bias conditions have been done using TDTW model and the reported DDE results were fully confirmed.

We have to point out that both the spontaneous emission and the background noise are included in our simulation. However, they do not result in visible instability in ES ML even when a large positive net gain window appears at pulse leading edge in the second operating condition. This phenomenon can be attributed partially to the fast relative shift of ES pulse with respect to the background noise, which limits the amplification of the noise before being merged with the pulse [74].

3.5.3 Sole ES ML

It can be seen from Fig. 3.22a and 3.22b that sole GS ML is established almost immediately after the onset of GS lasing. Then it is important to identify the reason why the sole ES ML cannot instead be achieved in the device with $\alpha_i = 2.2$ cm^{-1} at any of the investigated bias conditions and only continuous wave ES lasing is observed. Two main reasons are responsible for this result.

In Section 3.1, the S parameter has been introduced. For the device with $\alpha_i = 2.2$ cm^{-1}, GS lasing happens first, so dg_{GS}/dn and dg_{ES}/dn are calculated at the threshold carrier density of the GS $n_{GS,th}$; and the computed S parameter using Eq. (3.4) is 95 and 0.84 for GS and ES respectively. Therefore, it is clear that sole ES ML cannot be obtained in this device, since S_{ES} is less than one in this case, which means that the gain section is

even easier to be saturated than the SA for ES.

Besides the requirement in the S parameter, enough pulse energy to saturate the SA is also essential to form a pulse. For pulses longer than the time scale governing the recovery of a quasi-equilibrium distribution in the QD layers, the absorber saturation energy $E_{k,\mathrm{sat,SA}}$ (k= GS or ES) can be estimated using Eq. (3.2) [105]:

According to Fig. 3.20b and Eq. (3.2), $E_{GS,\mathrm{sat,SA}}$ is found to be only 1.4 pJ while $E_{ES,\mathrm{sat,SA}}$ is found to be approximately 7 pJ. Consistently with above values, GS ML happens almost immediately above its lasing threshold, while sole ES ML is not achieved since the onset of the ES-induced GS lasing requires a ES optical energy which is even smaller than $E_{ES,\mathrm{sat,SA}}$. Therefore, when current increases, the maximum accumulated ES optical energy before the onset of GS lasing is still not high enough to sufficiently saturate the ES absorption.

To conclude, in this section, the competition between GS and ES ML regimes in two passively mode locked lasers has been simulated with a modified MS-DDE approach. The reported operations have been fully explained from the results of the investigations of the gain and absorption steady-state and dynamic properties for InAs/InGaAs QD medium. Regarding the ML quality, we demonstrated not only the experimentally observed unstable dual-state ML, but also a stable dual-state ML regime at high injection current and reverse voltage, with significant improved peak power and pulse width.

3.6 Conclusion

In this chapter, a typical kind of QD-based monolithic laser, i.e., the passively mode-locked laser, has been comprehensively investigated via the FDTW and the MS-DDE models.

Based on the study of the fundamental analytic concepts governing the ML formation, ML lasers with and without the same value for the stability parameter S have been compared separately.

Various methods, such as increasing the SA length, changing the gain section to tapered shape and varying the number of the QD layers involving in the device active region, have been exploited to achieve higher S value in one device. Our simulation results confirm that if letting the device operate at a working point with high S where the gain is much harder to be saturated than the absorption, ML regime with high power, short width and better stability generally can be obtained. However, depending on the depth that one pushes the S parameter to high value, few drawbacks like trailing edge instability and early onset of lasing from ES transition may be encountered.

In addition, if keeping a fixed S, methods such as properly increasing the output reflectivity (increasing the SA length at the same time), increasing

the cavity total length and using the anti-colliding pulse mode-locking configuration still allow further improvements in the peak power or the pulse width of the obtained ML pulses. Our detail study of the intracavity pulse energy distributions in these device supply proper interpretation of above described results.

Comparison between the GS and ES MLs and the simultaneous GS&ES ML regime have also been discussed. We found that, with respect to the ES, it is always much easier to achieve lasing or ML from the GS. Especially, we demonstrated that at current and voltage well above the threshold, GS ML with significantly enhanced peak power, pulse width and stability is achieved under the help of the co-existing ES ML which has a locked group velocity as that for the GS pulses.

Chapter 4

CW longitudinally-varying QD devices

In Chapter 2, we introduced the FDTW and the DDE models for the QD-based semiconductor lasers and they were applied in Chapter 3 to study the QD-based lasers under ML regime. In these two models, the optical field is temporally and one-dimension-spatially resolved, so the optical field amplitude dynamics in the time domain and the varying along the longitudinal direction can be evaluated, such as the ML regime we studied in Chapter 3. However, these models neglect the variations of the optical field profile in both the lateral and the transversal directions and therefore only applicable to the QD devices with uniform cross-section. In practice, various devices with non-uniform cross-section, such as curvilinear directional couplers, branching waveguides, S-shaped bent waveguides and tapered waveguides are also indispensable components in constructing integrated optical circuits. Therefore, analysis techniques capable of solving optical field dynamics in longitudinally-varying devices are of paramount importance. Among the others, the beam propagation method is the most powerful technique to investigate the linear and nonlinear optical field propagation phenomena in such devices [106].

This chapter starts from the introduction of a finite-difference BPM (FD-BPM) model which is capable to simulate the QD-based devices with non-uniform cross-section (in Section 4.1). Then, in Section 4.2, this model is first used to investigate the gain-guided or weakly index-guided QD-based SOAs, which are used as parts of the master oscillator power amplifier (MOPA) system designed for the amplification of a stream of high power pulses. Later in Sections 4.3 and 4.4, studies of the anti-reflection efficiency and the QD-based straight or bent lasers are reported.

Results presented in this chapter have been obtained in the framework of the "Fast-Dot" European project.

4.1 Numerical modeling via FD-BPM

BPM has already been widely and successfully used to model the field evolution in 2D or 3D in longitudinally varying bulk and QW devices (see e.g. [107]). In this model, the local gain and the local refractive index are two of the most important parameters governing the optical field transformation along the propagation direction, and are usually simply related by the linewidth enhancement factor when modeling bulk and QW devices (see e.g. [108]). Although this approximation has been used also for QD materials (see e.g. [109]), it does not appear to be sufficiently precise in QD cases [36] when high saturation effect occurs. In this section, we propose a simple yet very effective way to extend the BPM model to describe QD devices by coupling it with the pre-calculated modal gain and refractive index obtained using multi-population rate equation (MPRE) system [59] which give a detailed description of the physical mechanisms that take place in QD materials and therefore is a self-consistent way to model the nonlinear variations of gain and refractive index. The BPM equation is solved based on the finite difference method, so we refer this model as the FD-BPM model.

The carrier concentration reduction, in the region of high photon intensity, will influence significantly both the modal gain and the refractive index, leading to the gain saturation effect [110] and the self-focusing effect [111] respectively. It is obvious that these two effects will play an important role in determining the device performances, i.e., the output power and beam quality, and have been studied separately using simplified models in previous papers [110], [112], [113], [114]. Unlike them, the joint influence of the modal gain and refractive index variation on the device characteristics can be investigated effectively using the proposed model; the results are presented in following sections.

In this chapter, we considered both gain-guided and index-guided QD-based devices, which are used as parts of the optical source systems for the generation of a stream of high power pulses. For this kind of application, few reasonable approximations are made to reduce the computational cost of this model. First, output from the mode locked laser usually has an average power in the range of mW indicating that the QD SOA operates at high gain saturation regime; this hypothesis allowed us to neglect the amplified spontaneous emission (ASE) which is strongly suppressed in this case. Secondly, a CW approximation is used since the applications we are addressing involve high power pulses with high repetition frequency (in the scale of GHz) and therefore the average input power is the parameter that should be taken into account.

It must be pointed out that although this model evaluate the field dynamics only in the lateral and the longitudinal directions, it can also be applied directly to generate more rigorous approach where 3D propagation and opto-thermal effects are considered.

Electric field evolution

The complete description of the electric field evolution in a 3D device has been approximated in this model by the combination of the effective index method (EIM) and FD-BPM. The former is exploited to simplify the computation task of field evolution from 3D to 2D and then the latter is used to propagate electric field in the lateral-longitudinal (X-Z) plane.

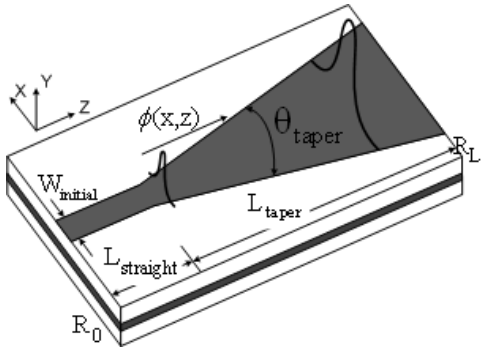

Figure 4.1: Schematic of a symmetric tapered SOA.

Figure 4.1 gives for example a schematic illustration of the geometry of a tapered symmetric semiconductor QD SOA, where $\phi(x,z)$ is the forward propagating electric field, R_0 and R_L are the residual facet power reflectivities at $x = 0$ and $x = \mathrm{L}$ respectively. The coordinates definition in this figure is valid throughout this chapter.

The 2D wave equation for the slowly varying components of the electric field $\phi(x,z)$ in QD material is based on the well known BPM second order differential equation (see e.g [106], [115]), which is derived from the Maxwell's equations Eq. (2.1):

$$\begin{aligned}\frac{\partial\phi}{\partial z} = &-j\frac{1}{2k_0n_0}\frac{\partial^2\phi}{\partial x^2} - j\frac{k_0}{2n_0}\left[n_i(x,z) + \Delta n(x,z,J,|\phi|^2) - n_0\right]^2\phi(x,z)\\ &+ \frac{1}{2}g(x,z,J,|\phi|^2)\phi(x,z) - \frac{1}{2}\alpha_i(x,z)\phi(x,z)\end{aligned} \tag{4.1}$$

where $k_0 = 2\pi/\lambda_0$ is the propagation constant calculated at the reference wavelength λ_0, n_0 is the reference refractive index outside the active waveguide, α_i are the intrinsic waveguide losses, $n_i(x,z)$ is the passive waveguide effective refractive index profile (obtained using EIM), $\Delta n(x,z,J,|\phi|^2)$ and $g(x,z,J,|\phi|^2)$ are, respectively, the modal gain (or absorption) and the refractive index variation induced by interaction between carriers and photons.

The first term in the right hand side of Eq. (4.1) represents the free space propagation in the medium with reference refractive index n_0, while

the following three terms determine the propagation of the confined field in the waveguide with linear (n_i) and nonlinear (g, Δn) effects and the intrinsic losses α_i.

For the longitudinally non-uniform device we considered, both the modal gain and the refractive index depend on the lateral and longitudinal positions, x and z. In addition, beside the dependence of local injected current density $J(x, z)$, they vary also according to the local photon density $S(x, z)$ (proportional to $|\phi(x, z)|^2$), due to the saturation effect that can be attributed to the finite intraband carrier relaxation rates of the QD material. Particular attention has to be paid to the calculation of $g(J, |\phi|^2)$ and $\Delta n(J, |\phi|^2)$ as described in next part.

Gain and refractive index variation

Since we consider only the CW emission regime, the dependence of the modal gain and the refractive index variation on the injection current density and the photon density ($g(J, |\phi|^2)$ and $\Delta n(J, |\phi|^2)$) are calculated in advance by searching for the stationary solution of a multi-population rate equation system which is more complex than the single-population rate equation system shown in Section 2.3 when setting J and S to fixed values. This MPRE system, although is more complex, has similar structure of that in Section 2.3, the differences just come from that the entire QD ensembles are divided into several sub-groups and QDs are identical in each sub-group. Explicit description of this rate equation system can be found in [24].

By solving this MPRE system in stationary condition for a discrete set of current densities J and photon densities S, we obtain the carrier occupation probabilities in the confined states of each QD sub-group, which are in turn used to calculate the QD susceptibility spectra $\chi(\lambda, J, S)$. Since the field is assumed to be monochromatic with the chosen reference wavelength λ_0, the modal gain $g(\lambda_0, J, S)$ and the refractive index variation $\Delta n(\lambda_0, J, S)$ can be computed simply by evaluating the imaginary and real part of the susceptibility spectra at λ_0.

An example of the result of these computations is shown in Fig. 4.2, demonstrating how the optical gain and refractive index change with the increases in the photon density and injection current. Saturation effect can be clearly observed at the region where optical power is high. For moderate optical power, the gain or absorption is always reduced, whereas the index changes can be positive or negative depending on the current density level; when the optical power is further increased, both of them go consistently to zero. Moreover, despite the small increase in the refractive index for very low J, a significant increase of the gain and a reduction of the refractive index are found when the current density J is increased. It can also be concluded from Fig. 4.2a that the gain saturation onset is slightly increased, i.e., the -3dB saturation density S_{sat} is larger, by increasing injection current.

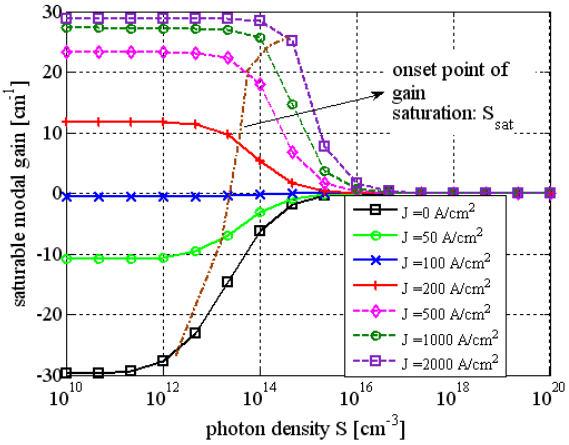

(a)

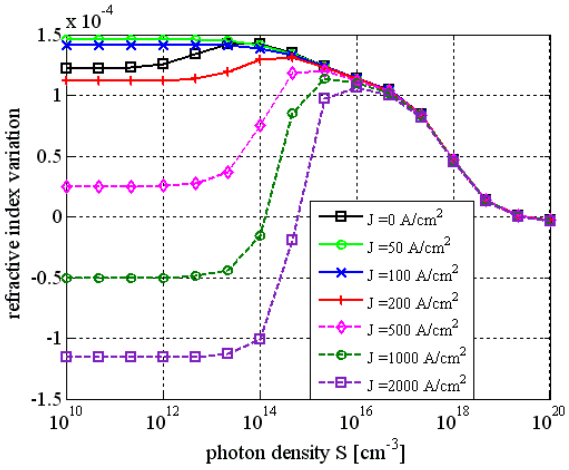

(b)

Figure 4.2: Example of modal gain g (a) and refractive index variation Δn (b) obtained for 15 dot-in-a-well layers material operating at about 1.3 μm, for different values of the injected current density J and photon density S.

These nonlinear behaviours of both the gain and the refractive index will significantly influence the optical field amplification in QD-based devices.

Numerical simulation approach for unidirectional SOAs

In the axially varying waveguides, the optical wave propagates in the planar waveguide with evolution in the lateral distributions. The optical amplitude, the carrier density, the gain variation and the carrier-induced refractive index variation are functions of both the longitudinal coordinate z and the lateral coordinate x. Therefore, a proper 2D simulation window

should be defined, which has the same length as the device but a larger width in order to guarantee that the electric field almost goes to zero at the window border. Transparent boundary conditions are used at the upper and lower borders of the simulation window to eliminate the non-realistic inward-propagating wave [116]. $R_0 = 0$ and $R_L = 0$ are assumed at the left and the right borders. The structure is discretized with a Cartesian bi-dimensional grid, being Δz and Δx the unit step in the longitudinal and lateral directions respectively, as shown in Fig. 4.3a, where we take a tapered SOA for example.

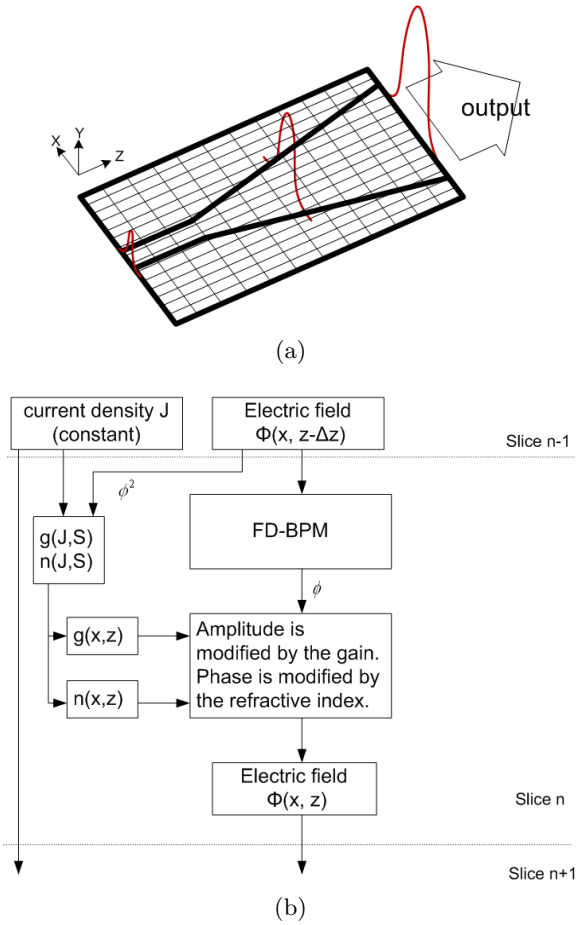

Figure 4.3: (a) Schematic of the simulation window. (b) The block diagram of the simulation procedure for a unidirectional SOA in one step.

The simulation is performed iteratively to propagate the field $\phi(x, z)$ from z to $z + \Delta z$ and Eq. (4.1) is numerically solved by approximating the differential operator by the corresponding incremental ratio over the 2D grid; this yields to a well-known tri-diagonal system which can be solved very efficiently. At each node of current lateral slice, the local modal gain

$g(x,z)$ and the local refractive index variation $\Delta n(x,z)$ are calculated by interpolating the values of pre-calculated $g(\lambda_0, J, S)$ and $\Delta n(\lambda_0, J, S)$ curves at the operating current density $J(x,z)$ and the local photon densities $S(x,z)$. Details of the numerical finite difference approach to solve the second order differential equation Eq. (4.1) can be found in [106].

As schematically shown in Fig. 4.3b, simulation of a QD SOA is performed in each longitudinal slice. The constant current density and the optical intensity distribution in prior slice are used to calculate the new gain and new index profile for the current slice. Then, they are inserted into the BPM wave equation Eq. (4.1), where the electric field amplitude is modified by the gain and the phase is modified by the refractive index to obtain the new optical intensity profile for the current slice. Then we move to the next slice. Once the initial electric field distribution at the input position $\phi(x, z = 0)$ is given, by successively performing this process along the beam propagation direction, we can finally get the electric field profile at the output facet.

In each slice z, the lateral carrier diffusion effect is included quantitatively by applying a *sliding window average operator* on $g(x,z)$ and $\Delta n(x,z)$ with a properly chose window width (we used 4 μm in following investigations, in order to get similar carrier distribution as that obtained using another commercial tool which calculates explicitly the carrier distribution in the transversal plane).

Under the CW operation condition, the carrier distribution in the confined state of each node in the simulation window is independent of time. So by calculating the steady state $g(\lambda_0, J, S)$ and $\Delta n(\lambda_0, J, S)$ curves before the iterative solution process of the field propagation, we can obtain the entire electric field distribution with relatively low computational cost. Therefore, this FD-BPM model represents a powerful simulation approach which can be applied in CW analysis and design of QD SOAs. However, one should notice that proper selection of the simulation window and the simulation steps in lateral and longitudinal directions is needed to ensure accuracy and short computational cost at the same time.

Numerical simulation approach for FP cavity lasers

In order to simulate the laser, both the forward and the backward propagating fields should be considered. Therefore, two equations like Eq. (4.1) have to be solved, one for the forward propagating optical field $\phi^+(x,z)$ and another for the backward propagating optical field $\phi^-(x,z)$. Furthermore, unlike that for the unidirectional SOA, in the FP laser case, the local modal gain and local effective refractive index variation should be calculated at each grid point as a function of the current density J and the total local photon density, which is proportional to $|\phi^+(x,z)|^2 + |\phi^-(x,z)|^2$.

In the FDTW model, evolutions of the forward and backward propa-

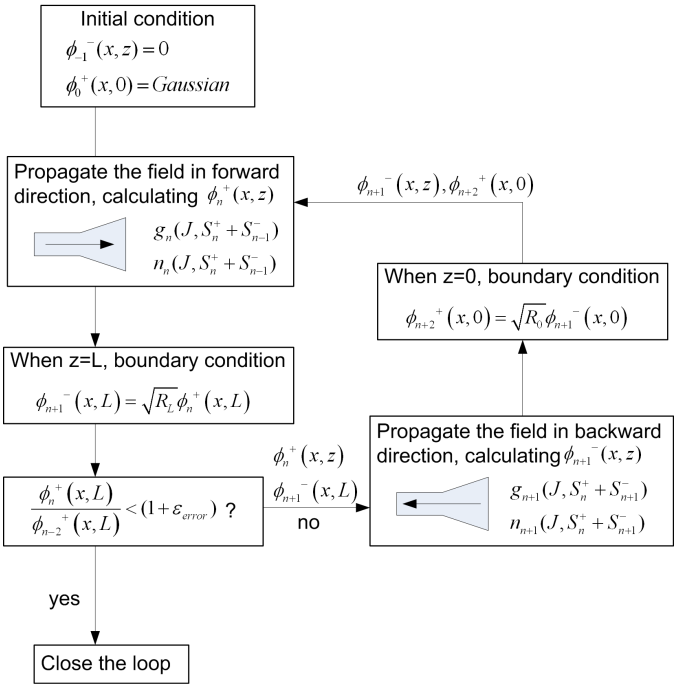

Figure 4.4: The block diagram of the simulation procedure for a FP cavity laser.

gating fields are calculated simultaneously. In this FD-BPM model, they are evaluated successively until a self-consistent solution for the optical field within one complete round-trip in the cavity is achieved. The stable self-consistent solution of the electric field can be found by following the algorithm presented below (see also Fig. 4.4). One propagation iteration means the optical field forward or backward passes through the entire cavity once.

1 The electric field $\phi_n^+(x,z)$ at the nth iteration is propagated in the forward direction assuming as backward field the distribution $\phi_{n-1}^-(x,z)$ obtained in the n-1th propagation iteration. So the total local photon density for this iteration is $S_n^+ + S_{n-1}^-$. When n=0, $\phi_{-1}^-(x,z)$ equals to 0, and the initial guess of the electric field at the input facet $\phi_0^+(x,0)$ is a Gaussian profile field with proper spot size for gain-guided device, or is assumed to be the fundamental mode of the input waveguide for index-guided device.

2 When the forward electric field $\phi_n^+(x,z)$ reaches the right facet, $z=L$, the boundary condition is applied $\phi_{n+1}^-(x,L)=\sqrt{R_L}\phi_n^+(x,L)$ and the initial field of the backward propagation $\phi_{n+1}^-(x,L)$ is generated.

3 The electric field $\phi_{n+1}^-(x,L)$ is propagated in the backward direction, assuming the just calculated $\phi_n^+(x,z)$ as the forward field distribution. So the total local photon density for this iteration is $S_n^+ + S_{n+1}^-$.

4 When z=0, we apply the boundary condition $\phi^{+}_{n+2}(x,0) = \sqrt{R_0}\phi^{-}_{n+1}(x,0)$. Then the procedure goes back to step 1.

This loop is performed iteratively, until the output field variation ϵ_{error} at the right facet $z = L$ after one complete round-trip is less than a user-specified tolerance.

Generally, the convergent field distribution could be found within 10 round trips. However, for certain device configurations or bias conditions, the convergence criterion can not be achieved (or hardly achieved depends on the required tolerance), since the device works in an unstable condition, for example, when strong filamentation appears. In this case the relative variation of output field after one complete round-trip doesn't decrease monotonically to zero, but fluctuates.

4.2 Investigation of tapered SOA

Semiconductor optical amplifiers offer various applications in optical communication systems, including direct amplification of optical signals as an optical power booster, and also applications as a power amplifier to implement a high power laser source. They can also be used to realize other functions such as optical wavelength conversion, wavelength filtering, and optical phase conjugation.

In "Fast-Dot" project, the MOPA structure is utilized aiming to achieve extremely high power optical pulse from the QD-based devices. The MOPA system consists actually of two autonomously operating devices, i.e., a semiconductor laser oscillator and an semiconductor optical amplifier. The passively ML laser investigated in Chapter 3 can be used as an oscillator, generating well shaped continuous pulse train. While the tapered SOA which will be discussed in this section is used as the optical power amplifier.

In this section, we present the investigation results of the tapered quantum dot semiconductor optical amplifiers in continuous wave high saturation regime using above illustrated FD-BPM model which includes in a rigorous way the nonlinear gain and refractive index variations in the semiconductor gain medium caused by saturation effects in QD. Using this model, a comprehensive analysis of the symmetric tapered QD SOAs is reported, verifying the influence of saturation effect on the characteristics of such devices and optimizing the design of both gain and weakly index-guided (WIG) structures for operating in high saturation regime.

4.2.1 General properties and design strategies

With respect to their application as a linear optical power amplifier, the QD-based SOAs exhibit broad spectral amplification bandwidth and low chirp at the same time [117]. However the inhomogeneous broadening of

the QD ensemble and the small active volume of QD heterostructure lead to relatively low modal gain of QD-based SOA, therefore requiring very long cavity and high injection current [118]. Nevertheless, the heat problem and the catastrophic optical damage (COD) problem still limit the achievement of high output power.

To overcome the drawbacks of low output power and COD, in principle, high power optical beam can be achieved by using a broad area gain region. However, in this kind of device, the beam deterioration due to nonlinear effects, such as filamentation, is the practical limiting factor at high power. The physical reason of the filamentation can be attributed to several factors. First, fluctuation of optical beam intensity leads to non-uniform gain depletion and also spatial variation of the carrier distribution, which in turn further enhances the gain to vary spatially, leading to effect like spatial hole burning. In addition, the variation of carrier distribution also results to spatial varying of the refractive index. And the associated self-focusing arising from spatial-dependent refractive index profile breaks up the lateral mode profile into multiple filaments.

Tapered SOA is one of the many different designs proposed to achieve a high power semiconductor source with still a relatively good beam quality [119], [**?**]. This design strategy has attracted particular attention also for providing a low cost, technological simple, yet effective device geometry suitable for high power and high brightness operation [90]. However, using this strategy, the local gain saturation and refractive index variation, which are important factors affecting the device characteristics of the QD-SOAs, should be properly treated. Therefore, careful design of the material epitaxy and the device geometry is still essential to delay the onset of the filamentation in a tapered SOA.

A typical tapered SOA, as shown in 4.1, consists of a ridge waveguide and a tapered section. The beginning straight section is designed to ensure a single spatial mode which will launches into the tapered section, and to filter out the undesired radiations coming from input optical field. Then, the single mode optical field diffracts during the propagation along the tapered section, lowing the optical intensity. The relatively low optical intensity in the gain section reduces the impact of nonlinear phenomena related to the spatial hole burning effect and the self-focusing effect, so maintaining the beam quality.

In addition, to avoid undesired lasing caused by back-reflection into the waveguide mode, both end facets of the practical SOAs are tilted, inhibiting lasing and allowing for single-pass amplification of the pumping source. However, in our numerical simulation, we consider the SOA as perpendicular to the simulation window. Primary test simulation confirms the validation of this assumption. The tapered active region also has the effect to reduce the back-reflection of the optical field, this property will be discussed in Section 4.3.

The above descriptions are the basic ideas behind tapered SOA design. However, although these ideas seem to be quite simple, complete underlying physics are complex. Accurate numerical models are therefore desirable not only to understand the strong nonlinear dynamics happening in high power SOAs, but also to supply reliable predictive designs and help the manufacturers to improve device performances.

4.2.2 Simulation of a typical tapered SOA

In this subsection, we consider a gain-guided SOA, which as schematically shown in Fig. 4.1 has total length $L_{total} = 6$ mm, consists of a 0.5 mm long 14 μm wide uniform input section and a tapered section with length $L_{taper} = 5.5$ mm and full taper angle $\theta_{taper} = 0.5°$, and operates at a wavelength of about 1.3 μm. The initial width of the SOA uniform section is chosen based on the criterion that higher order modes should be filtered out, but at the same time, modal gain should be as high as possible. The gain-guiding active region is defined by applying proton bombarding at the outside region (described in Section 1.3). The device we considered consists of 15 InAs/$In_{.15}Ga_{.85}As$ dot-in-a-well layers, as a material with larger number of QD layers generally presents higher gain and higher saturation density S_{sat}. The current is supposed to be uniformly injected below the contact layer. The model parameters required as input to the MPRE analysis for $g(\lambda_0, J, S)$ and $\Delta n(\lambda_0, J, S)$ can be found in [59].

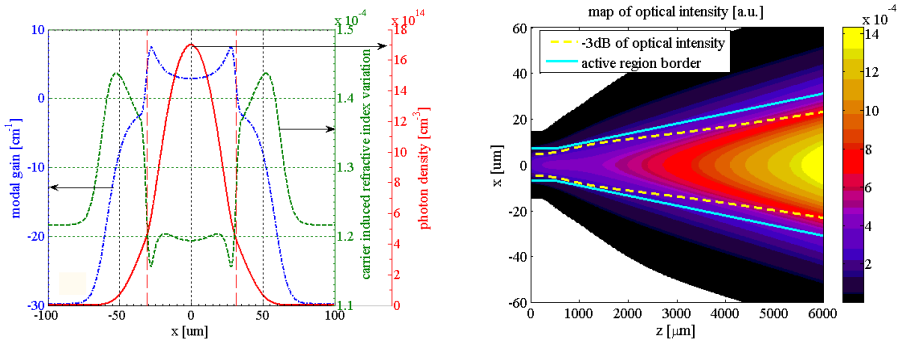

(a) (b)

Figure 4.5: Simulation results of a 0.5 degree tapered GG SOA when input optical power $P_{in} = 15$ dBm and injection current density $J_{in} = 650$ A/cm^2: (a) Lateral distribution of photon density (solid curve), modal gain (dotted curve) and carrier induced refractive index variation (dashed curve) at SOA output section (when $z = 6$ mm). Two vertical dashed lines indicate the local width of the active region; (b) Optical intensity map in XZ plane, with solid lines indicating device active region, and dashed lines indicating the -3 dB contour of the optical intensity. Optical intensity is shown in white when it is lower than 10^{-7}.

In Fig. 4.5a, the photon density distribution of this 6 mm long tapered GG SOA, when optical input power is $P_{in} = 15$ dBm and injection current density is $J_{in} = 650$ A/cm^2, is shown at SOA output section with the corresponding saturated gain and refractive index profiles. We can see that the optical field is well confined within this waveguide due to: the gain guiding effect, which restricts the optical field within the border of the active region by absorbing photons outside and amplifying photons inside; and the carrier-induced refractive index variation, which forms an internal weakly index guiding waveguide inside the active region and helps to further focus the optical field. Referring to Fig. 4.2, when the optical intensity increases, the guiding strength of the gain effect decreases due to gain suppression. On the contrary, the self-focusing strength, arising from the refractive index variation, increases due to enhanced index guiding profile.

These two guiding effects just identified are essential when we interpret the optical intensity distribution in the XZ plane (Fig. 4.5b). Just after the uniform section, the optical field diffracts during the propagation in the tapered section, lowering the optical density and allowing the field approaching the waveguide border; as the optical intensity is still low now, the gain guiding effect becomes dominant. When optical intensity increases, the refractive index self-focusing effect starts to supply visible contribution in the optical field confinement, i.e., forces the field to be apart from the waveguide border gradually.

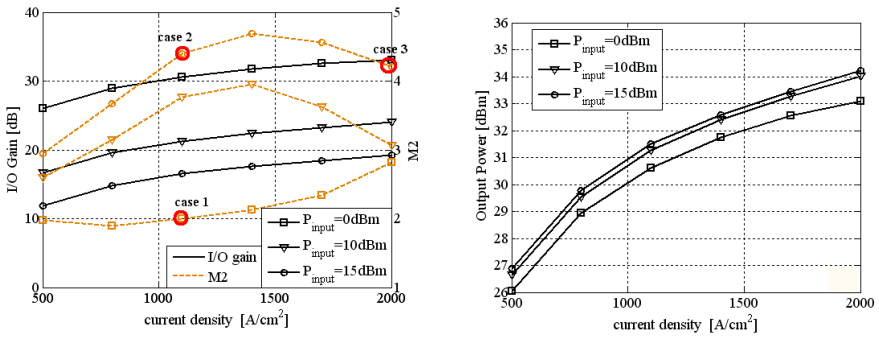

(a) (b)

Figure 4.6: SOA performances: in (a), the Input/Output gain (continuous lines) and the beam quality factor $M2$ (dashed lines); in (b), the output optical power under different injection current densities when the input excitation optical power is $P_{in} = 0$ dBm (square marker), 10 dBm (triangle marker) or 15 dBm (circle marker). Device layout parameters are the same as in Fig. 4.5. The numbered circles correspond to the bias and excitation cases discussed later in Fig. 4.7.

The performances of this 0.5 degree tapered GG SOA under different bias and excitation conditions are reported in Fig. 4.6 where the Input/Output gain $G_{I/O}$, the beam quality factor $M2$ [120] and the output power P_{out} have

been evaluated. As expected, $G_{I/O}$ decreases significantly with increasing P_{in} (Fig. 4.6a), and the reduction of $G_{I/O}$ almost compensates the difference in input power, therefore there is no significant change in the output power for various P_{in} we considered (Fig. 4.6b); but $G_{I/O}$ increases slowly when J_{in} increases (Fig. 4.6a) in the considered range. This behaviour is consistent with the properties of modal gain shown in Fig. 4.2a, and denotes that for such a long SOA the maximum achievable output power is almost independent of P_{in} (in fact, according to our simulation, for this 6 mm long SOA, the I/O chip gain decreases almost 10 dB/dec with respect to the input power at high saturation regime), but strictly limited by the gain saturation effect due to carrier depletion, which can be improved only with significant increase of J_{in}.

In order to give an interpretation of the $M2$ results in Fig. 4.6, we consider three cases to explain why the beam quality $M2$ increases significantly with the input power (from case 1 to case 2) and why it remains practically unchanged when increasing the current (from case 2 to case 3). To do this we report in Fig. 4.7 the refractive index, the gain and the photon density profiles computed at the input and output sections of the SOA. Being the structure and the excitation symmetric we report only the half left side of the input profiles and the half right side of the output profiles.

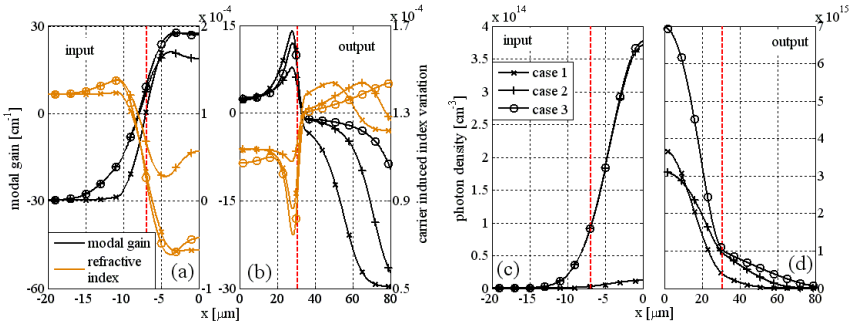

Figure 4.7: Input (when $z = 0$ mm) and output (when $z = 6$ mm) lateral profiles of the modal gain and the carrier induced refractive index variation (a, b) and the photon density distribution (c, d) for the three different operating conditions indicated in Fig. 4.6. For case 1: $P_{in} = 0$ dBm and $J_{in} = 1100$ A/cm^2 (x marker); for case 2: $P_{in} = 15$ dBm and $J_{in} = 1100$ A/cm^2 (plus marker); for case 3: $P_{in} = 15$ dBm and $J_{in} = 2000$ A/cm^2 (circle marker). Been the results symmetric only the results for $x < 0$ are reported for the input section and those for $x > 0$ in the output section. The vertical dashed lines represent the border of the waveguide width. Device layout parameters are the same as those in Fig. 4.5.

Being the considered input excitation relatively high (Fig. 4.7c), significant gain saturation effects can be already seen when comparing the results of case 1 and 2 (Fig. 4.7a), while in case 3 the higher injection compensates the saturation. An important difference between the considered cases is that

the lateral absorption saturation region in case 2 and 3 is wider than in case 1 due to the higher input power (Fig. 4.7a), which consequently lead to weaker gain guiding ability. Being the maximum output power difference of only 3 dB between the considered cases (Fig. 4.6b and also Fig. 4.7d) the saturation in the active region is similar at the output slice, while the absorption saturation region outside the injection region is growing from case 1 to case 3 (Fig. 4.7b). According to these considerations we can say that the increase of the $M2$ parameter with increasing input power is associated with an expansion of the lateral absorption saturation region; the practically constant $M2$ parameter found in the current interval between case 2 and 3 is manly due to the formation of a weakly index guiding waveguide caused by the reduction of the refractive index at the border of the injection region when moving from case 2 to case 3, which compensates to a certain extent the decrease of gain guiding ability due to wider absorption saturation in case 3 (Fig. 4.7b).

4.2.3 Performances improvement for tapered SOA

In this subsection two kinds of devices are investigated and optimized; one is gain-guided as that in the previous subsection and one is index-guided used to further improve the characteristics of the gain-guided one.

To compare device performances of different SOAs, we use as figure of merit the I/O gain corrected by the coupling efficiency of the output field:

$$G_{corrected} = G_{I/O}\beta_{coupling} \tag{4.2}$$

In our case according to [121], $\beta_{coupling}$ is calculated directly from the output beam quality factor $M2$ using the following equation:

$$\beta_{coupling} = \left[1 - \exp(-\frac{2}{M2})\right]^2 \tag{4.3}$$

This formula, used in our simulation, should/could be modified for other specific applications.

We have shown in Subsection 4.2.2 that the maximum output power is strictly limited by the gain saturation effect. Therefore, increasing the full taper angle is one possibility to achieve better device performance, e.g., higher gain, since the active region area is increased.

The results for the GG device considered in Section 4.2.2 by changing θ_{taper} are reported in Fig. 4.8. When we increase θ_{taper}, $G_{I/O}$ increases monotonically due to lower photon density in the wider active region and consequently gain saturation effects are weaker, while $M2$ does not show a monotonic variation, and achieve a minimum value at $\theta_{taper} = 0.4°$. Instead of analysing the independently changed $G_{I/O}$ and $M2$, we can now calculate

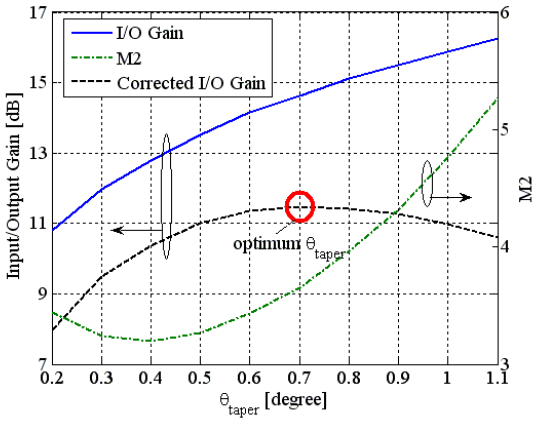

Figure 4.8: Variation of $G_{I/O}$ (solid line), $M2$ (dash-dotted line), and corrected I/O gain (dashed line) of the tapered GG SOA considered in Section 4.2.2 for different full taper angles θ_{taper} when P_{in} = 15 dBm and J_{in} = 650 A/cm^2.

the corrected I/O gain according to Eqs. (4.2) and (4.3) and show that θ_{taper} = 0.7° is the best taper angle for this GG tapered SOA.

Another possibility to improve the device performance is to introduce a WIG effect into the pure GG SOA in order to compensate the increase of the absorption saturation region discussed in the previous subsection. We assume to introduce a shallow ridge at the electrode border that allows a lateral current confinement and also produces a weak photon confinement by lowering the effective refractive index at the region outside the ridge.

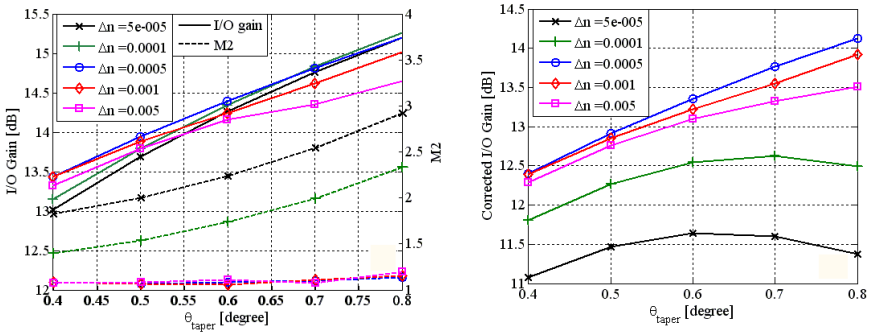

(a) (b)

Figure 4.9: WIG SOA characteristics: in (a), the Input/Output gain (solid lines) and the beam quality factor $M2$ (dashed lines); in (b), the corrected I/O gain of the tapered SOA considered in Section 4.2.2 for different full taper angles θ_{taper} and effective refractive index variations Δn when P_{in} = 15 dBm and J_{in} = 650 A/cm^2.

Fig. 4.9 shows the device characteristics with different θ_{taper} and IG

strength Δn. The curves for I/O gain and $M2$ in Fig. 4.9a display a qualitatively similar trend as those in Fig. 4.8 when θ_{taper} is changed. For $\theta_{taper} > 0.4°$, both I/O gain and $M2$ tend to increase as θ_{taper} is increased. However, when we change Δn from $5*10^{-5}$ to $5*10^{-3}$, although $G_{I/O}$ does not show any significant improvement with respect to the old results of GG SOA in Fig. 4.8, $M2$ is reduced significantly. Fig. 4.9a shows that $\Delta n = 5*10^{-4}$ is the optimum case respect to $M2$ because a further increase of Δn will not lead to any substantial reduction in $M2$. In addition, this choice can also allow to obtain the highest $G_{corrected}$ (Fig. 4.9b) and to guarantee approximately mono mode operation at the input linear section being the waveguide V number only 1.3π in this case.

It should be pointed out that, although $G_{corrected}$ shows continuous increase trend for larger θ_{taper}, it is not sufficiently correct to say that the larger the θ_{taper}, the better the device performance. As studied in [122], stripe width shows an important role in destabilizing the lateral mode and producing filamentation. Therefore, certain trade off should be made between high gain and stable operation during practical design.

In this section, we demonstrated the usage of the FD-BPM model to the investigation of the tapered SOAs working at high gain saturation regime. For this kind of device, the gain variation, as well as the refractive index variation, plays a dominant role in determining the output power and the output beam quality. Output power of long SOA is strictly limited by the gain saturation effect and the output beam quality is determined by complicated collaboration of the gain guiding effect and the self-focusing effect arising from the gain and refractive index variation. Furthermore, we also demonstrated the possibility to optimize the corrected gain in SOA by changing the full taper angle, or alternatively by introducing weakly index guiding effect. The corrected gain has been introduced in the optimization process as a figure of merit.

4.3 Study of end facet back-reflection

In above section, simulations of the single-passing SOA via FD-BPM model use a simulation widow with exactly the same length as the real device. Whereas in this section, we show for example another implementation of the FD-BPM model with a simulation window of two-fold long as the considered device. This approach is used to study the possibility for facet back-reflection reduction by using the tilted end facet and the tapered active region.

In order to evaluate the anti-reflection ability of a tapered and tilted structure, we need to measure the power reflected back into the waveguide. This phenomenon can be evaluated by the BPM simulations using the layout shown in Fig. 4.10, where the field is propagating continuously in one di-

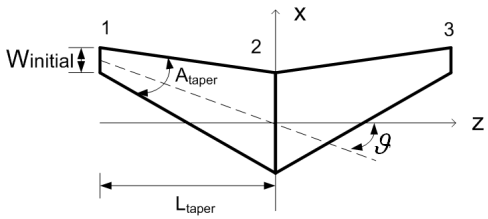

Figure 4.10: Simple schematic of the device structure used in the facet anti-reflection ability analysis.

rection in the whole window, but since we consider in the right half window a horizontal flipped part, this is equivalent to simulate also the backward propagating wave.

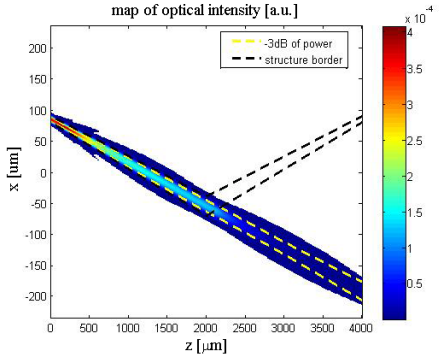

Figure 4.11: Optical intensity map in XZ plane, with solid lines indicating device active region, and dashed lines indicating the -3 dB contour of the optical intensity. Optical intensity is shown in white when it is lower than 10^{-7}.

The considered tapered section has initial width $W_{initial} = 10$ μm, the refractive index difference between the core and the cladding $\Delta n = 5{*}10^{-4}$. The full tapered angle A_{taper}, the tapered section total length L_{taper} and the end facet tilting angle ϑ will be varied. Furthermore, in order to study the device performances under the worst condition, we assume a 100% transmission at the middle interface 2, i.e., we have a 100% end facet reflectivity in the considered device. Therefore, we perform $\phi^{+}_{@2} = \sqrt{R}\phi^{-}_{@2}$ $(R = 1)$ at the middle interface for the electric field ϕ. To avoid the influence of the gain saturation effect, we also assume that the gain coefficient in the active region equals to 0 and the input power is very low.

The anti-reflection efficiency F is calculated according to:

$$F = \frac{(E_{@3}/E_{@1})}{(E_{@2}/E_{@1})^2} \tag{4.4}$$

where $E(z)$ is the optical power integrated over the active region at each longitudinal cuts.

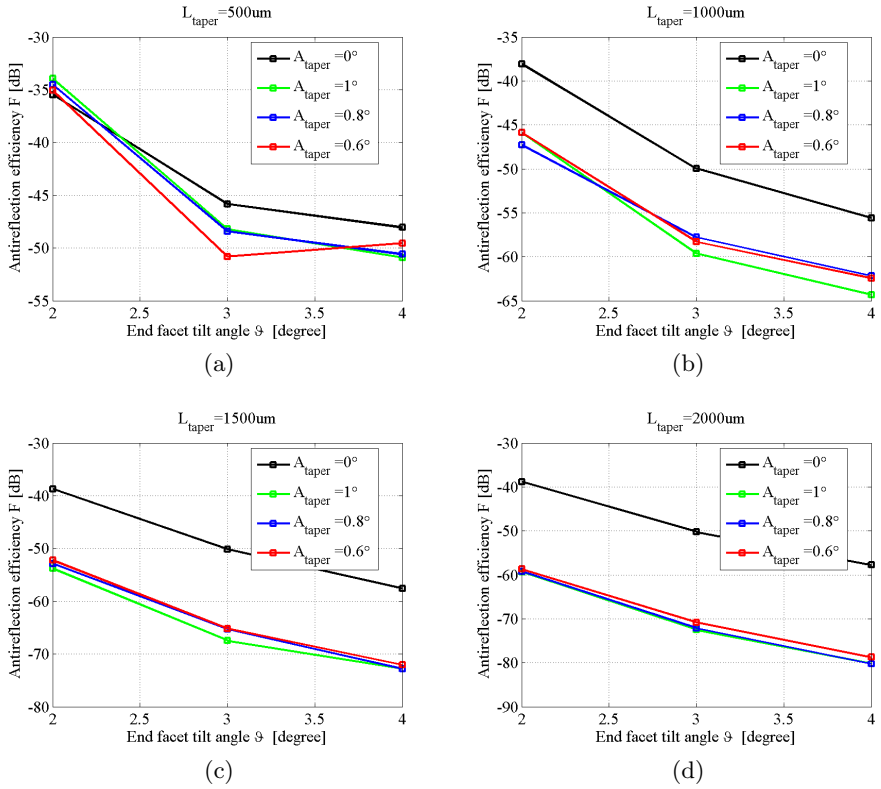

Figure 4.12: End facet anti-reflection efficiency F for tapered sections with length of 500 (a), 1000 (b), 1500 (c) and 2000 (d) μm.

Figure 4.11 shows as an example the simulated optical intensity map in the XZ plane. The coordinate limits correspond to the simulation window used in the numerical simulation. We can see that in this simulation, the optical field propagates still at its original incident direction after passing through the middle interface.

We report in Fig. 4.12 the variation of the anti-reflection efficiency when changing tapered section length, full taper angle and end facet tilting angle. Several features can be extracted from these simulation results:

- Influence of changing the length of the tapered section is almost negligible when $L_{taper} > 500$ μm.

- There is a significant reduction of the anti-reflection efficiency when using a tapered section instead of a linear section. This trend can be explained as follows. Since the optical field has a wider distribution at the end facet of the tapered section than that in narrow linear section, the Fourier transform of it, i.e., the angular spectrum of the optical field is narrower, and therefore in this case the reflected field has less

possibility to go back into the device.

- The anti-reflection efficiency decreases with increasing the end facet tilting angle.

In this section, waveguides as those depicted in Fig. 4.10, consisting of two replica of the tapered section under study, are investigated. We reported a systematic investigation of the anti-reflection efficiency using a tilted tapered section as the final part in a SOA. The simulation results demonstrated that extremely low back reflection ratio can be achieved by using this design even when there is no help from the anti-reflection coating.

4.4 Study of tapered QD-based laser

As a continuous extending of above two sections, we present in this section the simulation using the FD-BPM model for axially varying QD lasers, i.e., optical field is propagating back and forth in the laser cavity. Numerical approach of this kind of simulation has been described in Section 4.1.

Straight tapered laser

Single tapered laser can also be used to achieve large gain and good beam quality simultaneously. In this part, the laser simulation approach described in Section 4.1 is applied to the investigations of straight tapered lasers.

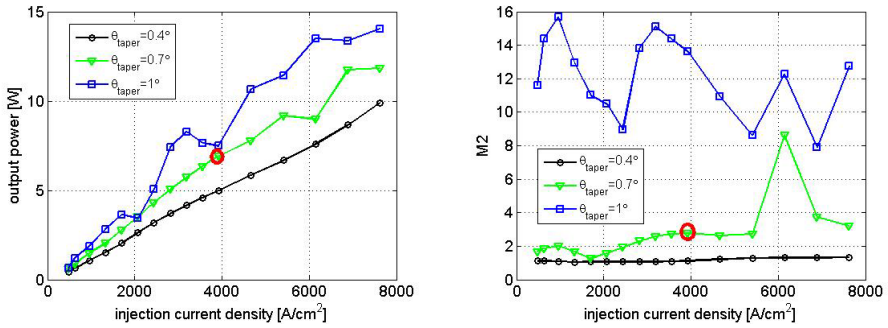

(a) (b)

Figure 4.13: PI characteristic (a) and M2 (b) for three WIG ($\Delta n = 5{*}10^{-4}$) straight tapered lasers with $\theta_{taper} = 0.4°$ (circle marker), $\theta_{taper} = 0.7°$ (triangle marker), and $\theta_{taper} = 1°$ (square marker). The red circle in the curve for $\theta_{taper} = 0.7°$ indicates the maximum current density that convergent results can be achieved.

Figure 4.13 shows the PI and M2 characteristics of a straight tapered WIG laser, with the optimized parameter set ($\theta_{taper} = 0.7°$ and $\Delta n =$

$5*10^{-4}$) obtained in Section 4.2.3 for the tapered SOAs, and with high-reflection coated front facet $R_L = 0.95$, and low-reflection coated back facet $R_0 = 0.03$. When $\theta_{taper} = 0.7°$, convergent result can be obtained for current density up to 4000 A/cm^2 (typically within 7 round trips). After that, however, severe filamentation starts to be observed, which can be attributed to strong self-focusing effect under large injection current, resulting in large fluctuations of ϵ_{error} along the iterative procedure and unstable lateral field profile. Hence, the simulation is forced to stop after 10 round trips, and a transient result is stored.

For comparison, two other cases with $\theta_{taper} = 0.4°$ and $\theta_{taper} = 1°$ are investigated also. Convergent result is achieved under all current densities we considered in Fig. 4.13 when $\theta_{taper} = 0.4°$. On the contrary, convergent result is never achieved when $\theta_{taper} = 1°$. This result indicates that strip width is tightly related with filamentation generation.

The optical output power is determined by the photon density summation at the back facet, whereas the $M2$ is determined by the shape of the output field. Therefore, in the case of $\theta_{taper} = 1°$, although influenced by the filamentation effect, output power increases with small fluctuation as the injection current density is increased (Fig. 4.13a), while $M2$ fluctuates randomly (Fig. 4.13b). Situation is the same when $\theta_{taper} = 0.7°$ after J_{in} = 4000 A/cm^2. For the case where convergent result is achieved, such as $\theta_{taper} = 0.4°$ and $\theta_{taper} = 0.7°$ before J_{in} = 4000 A/cm^2, the output power increases linearly with the injection current density and the $M2$ has almost a constant value.

Through this kind of simulation, qualitative prediction of the beam quality in a straight tapered laser operating under CW regime can be achieved. In addition, we can extract from these simulations the lateral confinement factor for the optical field propagating along the longitudinal direction, and then use this quantity as an input to the wave equation in the FDTW or the FD-DDE model for simulating tapered lasers operating under ML regime (as reported in Section 3.3.1).

Bent external cavity laser

Monolithically integrated ML laser has a fixed repetition rate defined by the cavity length $f = c/Ln_0$, usually referred as the fundamental frequency. Alternatively, harmonic ML obtained from a monolithic ML laser operates at a repetition rate as integer multiple of the fundamental frequency. As a route to achieve repetition rates below the lowest repetition rate obtained from such devices, an external cavity ML configuration can be employed. Although external cavity lasers (ECLs) are more complex with respect to monolithically integrated devices, they do offer a number of distinguish advantages, such as possibility of repetition rate tuning and the ability to include intra-cavity elements for wavelength tuning and dispersion

compensation [63], [70].

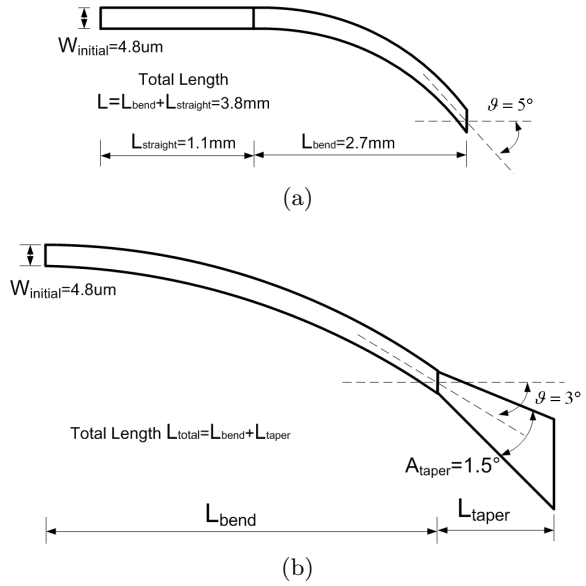

Figure 4.14: Schematics of the considered IG (Δn = 1.6*10^{-3}) bent lasers: (a) uniform bent laser and (b) bent laser with a tapered end section.

Typical ML laser with the external cavity configuration consists of a two-section ML laser diode, coupling lenses and a output coupler. Unlike the conventional design where the ML laser diode is straight, in the "FAST-DOT" project, we use a bent ML laser diode for pulse generation as shown in Fig. 4.14. With this design, the waveguide is perpendicular to the back facet allowing high reflection and is terminated with a certain angle to the front facet minimizing the back reflection from this facet (as we discussed in Section 4.3). Such configuration adds to the complexity of the pulse source when compared with the simple straight two-section ML lasers, therefore BPM simulation is employed to check primarily the guiding ability and the beam quality of the bent waveguide.

For a real ECL, the reflectivity of the front facet is very low and the laser cavity is actually defined by the external cavity output coupler which supplies sufficient reflection to achieve lasing. In the numerical model however, we simulate the field dynamics within the chip laser only and assume the optical field is reflected back from the front facet directly without further propagation in the external cavity. Therefore we set the front facet reflectivity value to the original reflectivity at the external cavity output coupler. Furthermore, in order to have a reflected field going back to the bent waveguide under a correct direction, the boundary condition at the front facet described in Section 4.1 should be changed to $\phi^{-}(x, L) = \sqrt{R_L}\phi^{+,*}(x, L)$ ($*$ means complex conjugate).

We consider as the reference a uniform bent laser with a straight sec-

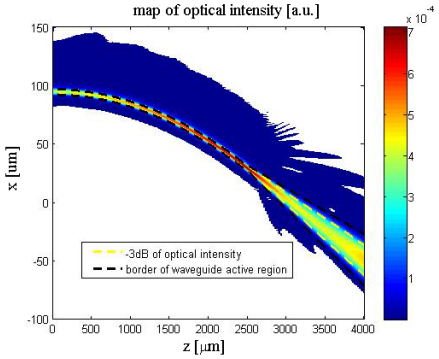

Figure 4.15: Optical intensity map in XZ plane, with solid lines indicating device active region, and dashed lines indicating the -3 dB contour of the optical intensity. Optical intensity is shown in white when it is lower than 10^{-7}.

tion of 1.1 mm long (this section can be used as the SA when operating under passively ML regime), a bent section of 2.7 mm long, the initial width $W_{initial} = 4.8$ μm, the back facet is high-reflection coated with a reflectivity of 95% and the front facet has reflectivity of 3%. The bent section terminates at an angle of 5° (Fig. 4.14a). The QD chirp contains 15 layers of self-assembled InAs/InGaAs QDs. The entire waveguide is index-guided with $\Delta n = 1.6{*}10^{-3}$. This configuration corresponds the bent ECL realized by our colleague Igor Krestnikov and coworkers from INNOLUME. Three additional bent lasers of different total lengths, incorporating a uniform bent section (parts of this section can be used as the SA to achieve passively ML regime) and a tapered section (Fig. 4.14b), are also considered: $L_{bent} = 1$ mm and $L_{taper} = 1.5$ mm, $L_{bent} = 1.5$ mm and $L_{taper} = 1.5$ mm, $L_{bent} = 2.5$ mm and $L_{taper} = 1.5$ mm. These three devices have the same full taper angle $A_{taper} = 1.5°$, final tilting angle $\vartheta = 3°$, and the same active region as the reference uniform bent laser. All the bent sections have circular curvature.

In Fig. 4.15, the optical intensity map when injection current equal to 0.2 A is shown for the $L = 4$ mm case. Obvious whispering gallery effect can be observed from this figure, i.e., the field is compressed mainly in the upper waveguide border region. Therefore, practically the attempt to use tapered bent structure starting from the back facet is not useful, since the area of effective amplification will be much smaller respect to the area of current injection. Thus, in our design the main part of the waveguide is uniform and the tapered section with limited length is used only to improve the anti-reflection ability at the front facet. Additionally, we also observe certain amount of optical power leakage from the active waveguide due to the bent geometry. This is the reason why we use such a large refractive index step between the core and the cladding to guarantee strong index-guiding effect, otherwise this power leakage will be enormous.

Figure 4.16 shows the PI and $M2$ characteristics of the considered bent

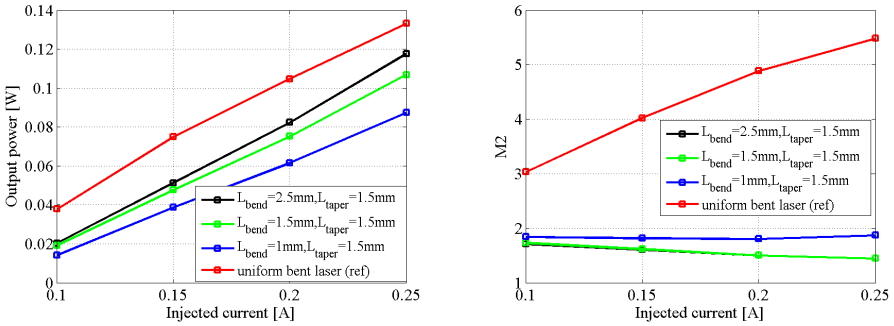

(a) (b)

Figure 4.16: PI characteristic (a) and $M2$ (b) for the considered four IG ($\Delta n = 1.6{*}10^{-3}$) bent lasers.

IG lasers. One can easily find that since the reference uniform laser has the smallest area, under same current injection level, the highest output power is achieved from this device. For the beam quality however, this device exhibits much higher $M2$.

4.5 Conclusion

In this chapter, a FD-BPM model suitable to simulate the axially varying optical devices is introduced. In this numerical model, we implemented in a rigorous and computational efficient way the modeling of gain saturation and carrier-induced refractive index variation effects.

Then, we illustrate several different applications of this model to the axially varying semiconductor devices, such as the investigation of single-passing tapered SOA, the study of the anti-reflection ability when using tapered and tilted section and the study of the straight or bent lasers with resonant cavity. These simulations put in evidence that this FD-BPM model is a reliable tool for analysing 2D optical field dynamics study and can be applied for a large number of applications.

Chapter 5

Conclusions and future works

In this thesis, we reviewed the main activities carried on during my Ph.D period under the framework of the "Fast Dot" EU project, aiming to achieve high-power ultra-fast laser sources based on novel quantum dot structures. Two classes of electro-optic devices, the passively ML lasers and the SOAs, have been investigated in collaboration with other partners in the "Fast Dot" project.

Well-defined pulse train with characteristic repetition rate in GHz scale can be obtained from a two-section passively ML laser only when the geometry and the bias condition of this device are all properly designed. Using the FDTW and the MS-DDE models, we studied the main physical mechanisms which exist in such devices and are responsible for the pulse formation. Then based on these studies, comprehensive investigations have been performed searching for the possibility to optimize the output performances of a ML laser. We verified that pulses with higher peak power or shorter pulse width can be achieved if we push the stable parameter S to higher value by increasing the SA length, introducing a tapered gain section or reducing the QD layers involved in device active region, and alternatively if we keep the same S value but increase properly the output reflectivity, or increase device total length, or put the SA close to the facet with high optical power extraction rate. The simulation results show good qualitative agreement with the experimental findings and give therefore reliable design guidance of the passively ML lasers.

Additionally, special attention have been paid to the dual-state ML regime in monolithic ML lasers which has been newly demonstrated by our partners at the University of Dundee (UK) and the Technische Universität Darmstadt (Germany). Efforts have been devoted to modify the original MS-DDE model to correctly describe the non-linear dynamics of GS and ES optical fields which travel with different group velocities in the laser cavity and their interactions with the carriers in the QD active medium. With this modified model, various lasing or ML regimes that could possibly been

observed in a two-section ML laser have been investigated and key reasons that trigger these regimes have been explained. Most of the simulation results are consistent with the experimental results both from the literatures and from our partners. However, we also observed one bias region with high voltage and high current, where the optical pulses from the GS and ES transitions propagate at the same group velocity and have extremely enhanced peak power, pulse width and stability. This special ML regime has not been demonstrated by any experimental group yet.

In the second part of this work, we focused on the design of tapered SOAs operating at high power regime. To this scope, a BPM model has been developed allowing a reliable description of the optical field propagation in an axially varying waveguide. Additionally, by combining the beam propagation equation with pre-calculated results obtained from the MPRE system, we could model in a rigorous and efficient way the non-linear gain and refractive index variation occurring in the QD active medium at high power regime. Using this model, the static properties of the GG and WIG tapered SOAs have been investigated. Our simulations helped other partners to design the high performance SOAs used in the MOPA structure for the amplification of a stream of high power pulses. The final realized laser systems show good quality in generating high-power, ultra-short optical pulses (see for example [70]).

We shown also the possible usage of this BPM model in other aspects of the electro-optic device design, such as to study the anti-reflection effect of a waveguide with tapered end section and tilted facet, and to simulate the lateral beam quality of a tapered laser from which useful information can be extracted and used as an input to the FDTW or MS-DDE model for the dynamic simulation of tapered ML lasers.

Actually, above mentioned three numerical models are all quite flexible and not sufficient to been restricted in the applications we demonstrated in this thesis. Therefore, future activities will be the further exploration of their usages in the design of QD-based optical devices. For example, the FDTW can be easily modified to study of the continuous wave or pulse propagation in QD SOAs. Furthermore, since there are a large number of simplifications and approximations when developing these models, we can cancel some of them or include additional terms in the numerical model to describe also other physical mechanisms in the QD devices, such as the thermal effects and the current lateral diffusion effects.

References

[1] R. N. Hall, G. E. Fenner, J. D. Kingsley, T. J. Soltys, and R. O. Carlson, "Coherent light emission from GaAs junctions," *Phys. Rev. Lett.*, vol. 9, no. 9, pp. 366–368, 1962.

[2] M. Okuda and K. Onaka, "Analysis of Distributed Bragg-Reflector Laser Amplifiers," *Jpn. J. Appl. Phys.*, vol. 16, p. 125, 1976.

[3] G. Evans and T. Wilcox, "Mode coupling and distributed feedback lasers in periodic fiber waveguides," *IEEE J. of Quantum Electron.*, vol. 13, no. 4, pp. 145–152, 1977.

[4] I. Hayashi, M. B. Panish, P. W. Foy, and S. Sumski, "Junction lasers which operate continuously at room temperature," *Appl. Phys. Lett.*, vol. 17, no. 3, pp. 109–111, 1970.

[5] R. Dingle, W. Wiegmann, and C. H. Henry, "Quantum states of confined carriers in very thin $Al_xGa_{1-x}As$ - GaAs - $Al_xGa_{1-x}As$ heterostructures," *Phys. Rev. Lett.*, vol. 33, no. 14, pp. 827–830, 1974.

[6] J. J. Coleman, J. D. Young, and A. Garg, "Semiconductor quantum dot lasers: A tutorial," *J. Lightwave Technol.*, vol. 29, no. 4, pp. 499–510, 2011.

[7] M. Asada, Y. Miyamoto, and Y. Suematsu, "Gain and the threshold of three-dimensional quantum-box lasers," *IEEE J. of Quantum Electron.*, vol. 22, no. 9, pp. 1915–1921, 1986.

[8] E. Bauer, "Phänomenologische theorie der kristallabscheidung an oberflächen. I," *Zeitschrift für Kristallographie*, vol. 110, no. 1-6, pp. 372–394, 1958.

[9] R. Murray, D. Childs, S. Malik, P. Siverns, C. Roberts, J.-M. Hartmann, and P. Stavrinou, "1.3 μm room temperature emission from InAs/GaAs self-assembled quantum dots," *Jpn. J. Appl. Phys.*, vol. 38, no. 1B, p. 528, 1999.

[10] J. Tatebayashi, M. Nishioka, and Y. Arakawa, "Over 1.5 μm light emission from InAs quantum dots embedded in InGaAs strain-reducing layer grown by metalorganic chemical vapor deposition," *Appl. Phys. Lett.*, vol. 78, no. 22, pp. 3469–3471, 2001.

[11] M. G. Thompson, A. R. Rae, X. Mo, R. V. Penty, and I. H. White, "InGaAs quantum-dot mode-locked laser diodes," *IEEE J. Select. Top. Quantum Electron.*, vol. 15, no. 3, pp. 661–672, 2009.

[12] I. R. Sellers, H. Y. Liu, K. M. Groom, D. T. Childs, D. Robbins, T. J. Badcock, M. Hopkinson, D. J. Mowbray, and M. S. Skolnick, "1.3 μm InAs/GaAs multilayer quantum-dot laser with extremely low room-temperature threshold current density," *Electron. Lett.*, vol. 40, no. 22, pp. 1412–1413, 2004.

[13] K. Mukai, Y. Nakata, K. Otsubo, M. Sugawara, N. Yokoyama, and H. Ishikawa, "High characteristic temperature of near-1.3 μm InGaAs/GaAs quantum-dot lasers at room temperature," *Appl. Phys. Lett.*, vol. 76, no. 23, pp. 3349–3351, 2000.

[14] S. Melnik, G. Huyet, and A. Uskov, "The linewidth enhancement factor of quantum dot semiconductor lasers," *Opt. Express*, vol. 14, no. 7, pp. 2950–2955, 2006.

[15] Z. Mi, P. Bhattacharya, and S. Fathpour, "High-speed 1.3 μm tunnel injection quantum-dot lasers," *Appl. Phys. Lett.*, vol. 86, no. 15, pp. 153 109–3, 2005.

[16] S. M. Kim, Y. Wang, M. Keever, and J. S. Harris, "High-frequency modulation characteristics of 1.3 μm InGaAs quantum dot lasers," *IEEE Photonics Technol. Lett.*, vol. 16, no. 2, pp. 377–379, 2004.

[17] N. Kirstaedter, N. N. Ledentsov, M. Grundmann, D. Bimberg, V. M. Ustinov, S. S. Ruvimov, M. V. Maximov, P. S. Kop'ev, Z. I. Alferov, U. Richter, P. Werner, U. Gosele, and J. Heydenreich, "Low threshold, large to injection laser emission from (InGa)As quantum dots," *Electron. Lett.*, vol. 30, no. 17, pp. 1416–1417, 1994.

[18] S. Franchi, G. Trevisi, L. Seravalli, and P. Frigeri, "Quantum dot nanostructures and molecular beam epitaxy," *Prog. Cryst. Growth Charact. Mater.*, vol. 47, no. 23, pp. 166–195, 2003.

[19] M. Sugawara, *Self-Assembled InGaAs/GaAs Quantum Dots.* Academic Press, 1999.

[20] T. Walther, A. G. Cullis, D. J. Norris, and M. Hopkinson, "Nature of the stranski-krastanow transition during epitaxy of InGaAs on GaAs," *Phys. Rev. Lett.*, vol. 86, no. 11, pp. 2381–2384, 2001.

[21] A. G. Cullis, D. J. Norris, T. Walther, M. A. Migliorato, and M. Hopkinson, "Stranski-krastanow transition and epitaxial island growth," *Phys. Rev. B*, vol. 66, no. 8, p. 081305, 2002.

[22] M. Krakowski, P. Resneau, M. Calligaro, M. Hugues, M. Hopkinson, M. Gioannini, P. Bardella, and I. Montrosset, "High power, broad spectral width, 1300nm quantum-dot superluminescent diodes," in *Semiconductor Laser Conference, 2008. ISLC 2008. IEEE 21st International*, pp. 23–24.

[23] V. M. Ustinov, N. A. Maleev, A. E. Zhukov, A. R. Kovsh, A. Y. Egorov, A. V. Lunev, B. V. Volovik, I. L. Krestnikov, Y. G. Musikhin, N. A. Bert, P. S. Kop'ev, Z. I. Alferov, N. N. Ledentsov, and D. Bimberg, "InAs/InGaAs quantum dot structures on GaAs substrates emitting at 1.3 μm," *Appl. Phys. Lett.*, vol. 74, no. 19, pp. 2815–2817, 1999.

[24] M. Rossetti, "Numerical modelling of light sources based on semiconductor quantum dots," *PhD thesis*, 2011.

[25] G. P. The, "Improved modeling and simulation of quantum dot lasers," *PhD thesis*, 2010.

[26] J. Kim, M. Laemmlin, C. Meuer, D. Bimberg, and G. Eisenstein, "Static gain saturation model of quantum-dot semiconductor optical amplifiers," *IEEE J. of Quantum Electron.*, vol. 44, no. 7, pp. 658–666, 2008.

[27] C. Z. Tong, S. F. Yoon, C. Y. Ngo, C. Y. Liu, and W. K. Loke, "Rate equations for 1.3 μm dots-under-a-well and dots-in-a-well self-assembled InAs-GaAs quantum-dot lasers," *IEEE J. of Quantum Electron.*, vol. 42, no. 11, pp. 1175–1183, 2006.

[28] K. Jungho, C. Meuer, D. Bimberg, and G. Eisenstein, "Numerical simulation of temporal and spectral variation of gain and phase recovery in quantum-dot semiconductor optical amplifiers," *IEEE J. of Quantum Electron.*, vol. 46, no. 3, pp. 405–413, 2010.

[29] ——, "Effect of inhomogeneous broadening on gain and phase recovery of quantum-dot semiconductor optical amplifiers," *IEEE J. of Quantum Electron.*, vol. 46, no. 11, pp. 1670–1680, 2010.

[30] N. Marcuvitz, *Waveguide Handbook*. Boston Technical Publishers, 1951.

[31] D. Marcuse, *Theory of dielectric optical waveguides*, 2nd ed. Academic Press, 1991.

[32] A. Snyder and J. Love, *Optical Waveguide Theory*. Chapman and Hall, 1995.

[33] S. Cortez, O. Krebs, P. Voisin, and J. M. Gerard, "Polarization of the interband optical dipole in InAs/GaAs self-organized quantum dots," *Phys. Rev. B*, vol. 63, no. 23, p. 233306, 2001.

[34] K. L. Silverman, R. P. Mirin, S. T. Cundiff, and A. G. Norman, "Direct measurement of polarization resolved transition dipole moment in InGaAs/GaAs quantum dots," *Appl. Phys. Lett.*, vol. 82, no. 25, pp. 4552–4554, 2003.

[35] M. Sugawara, H. Ebe, N. Hatori, M. Ishida, Y. Arakawa, T. Akiyama, K. Otsubo, and Y. Nakata, "Theory of optical signal amplification and processing by quantum-dot semiconductor optical amplifiers," *Phys. Rev. B*, vol. 69, no. 23, p. 235332, 2004.

[36] M. Gioannini and I. Montrosset, "Numerical analysis of the frequency chirp in quantum-dot semiconductor lasers," *IEEE J. of Quantum Electron.*, vol. 43, no. 10, pp. 941–949, 2007.

[37] A. Markus, M. Rossetti, V. Calligari, D. Chek-Al-Kar, J. X. Chen, A. Fiore, and R. Scollo, "Two-state switching and dynamics in quantum dot two-section lasers," *J. Appl. Phys.*, vol. 100, no. 11, pp. 113 104–113 104–5, 2006.

[38] M. Sugawara, T. Akiyama, N. Hatori, Y. Nakata, H. Ebe, and H. Ishikawa, "Quantum-dot semiconductor optical amplifiers for high-bit-rate signal processing up to 160 Gb/s and a new scheme of 3R regenerators," *Measurement Science and Technology*, vol. 13, no. 11, p. 1683, 2002.

[39] T. W. Berg, S. Bischoff, I. Magnusdottir, and J. Mork, "Ultrafast gain recovery and modulation limitations in self-assembled quantum-dot devices," *IEEE Photonics Technol. Lett.*, vol. 13, no. 6, pp. 541–543, 2001.

[40] W. W. Chow and S. W. Koch, "Theory of semiconductor quantum-dot laser dynamics," *IEEE J. of Quantum Electron.*, vol. 41, no. 4, pp. 495–505, 2005.

[41] W. W. Chow, H. C. Schneider, and M. C. Phillips, "Theory of quantum-coherence phenomena in semiconductor quantum dots," *Phys. Rev. A*, vol. 68, no. 5, p. 053802, 2003.

[42] T. R. Nielsen, P. Gartner, and F. Jahnke, "Many-body theory of carrier capture and relaxation in semiconductor quantum-dot lasers," *Phys. Rev. B*, vol. 69, no. 23, p. 235314, 2004.

[43] P. Blood, H. Pask, H. D. Summers, and I. Sandall, "Localized Auger recombination in quantum-dot lasers," *IEEE J. of Quantum Electron.*, vol. 43, no. 12, pp. 1140–1146, 2007.

[44] I. P. Marko, A. D. Andreev, A. R. Adams, R. Krebs, J. P. Reithmaier, and A. Forchel, "The role of Auger recombination in InAs 1.3 μm quantum-dot lasers investigated using high hydrostatic pressure," *IEEE J. Select. Top. Quantum Electron.*, vol. 9, no. 5, pp. 1300–1307, 2003.

[45] D. B. Malins, A. Gomez-Iglesias, S. J. White, W. Sibbett, A. Miller, and E. U. Rafailov, "Ultrafast electroabsorption dynamics in an InAs quantum dot saturable absorber at 1.3 μm," *Appl. Phys. Lett.*, vol. 89, no. 17, pp. 171 111–3, 2006.

[46] M. G. Thompson, C. Marinelli, Y. Chu, R. L. Sellin, R. V. Penty, L. H. White, M. Van Der Poel, D. Birkedal, J. Hvam, V. M. Ustinov, M. Lammlin, and D. Bimberg, "Properties of InGaAs quantum dot saturable absorbers in monolithic mode-locked lasers," in *IEEE 19th International Semiconductor Laser Conference, 2004*, pp. 53–54.

[47] A. D. Stiff-Roberts, X. H. Su, S. Chakrabarti, and P. Bhattacharya, "Contribution of field-assisted tunneling emission to dark current in InAs-GaAs quantum dot infrared photodetectors," *IEEE Photonics Technol. Lett.*, vol. 16, no. 3, pp. 867–869, 2004.

[48] P. W. Fry, I. E. Itskevich, D. J. Mowbray, M. S. Skolnick, J. J. Finley, J. A. Barker, E. P. O'Reilly, L. R. Wilson, I. A. Larkin, P. A. Maksym, M. Hopkinson, M. Al-Khafaji, J. P. R. David, A. G. Cullis, G. Hill, and J. C. Clark, "Inverted electron-hole alignment in InAs-GaAs self-assembled quantum dots," *Phys. Rev. Lett.*, vol. 84, no. 4, pp. 733–736, 2000.

[49] C. H. Henry and R. F. Kazarinov, "Quantum noise in photonics," *Rev. Mod. Phys.*, vol. 68, no. 3, pp. 801–853, 1996.

[50] K. Böhringer and O. Hess, "A full time-domain approach to spatio-temporal dynamics of semiconductor lasers. II. spatio-temporal dynamics," *Prog. Quantum Electron.*, vol. 32, no. 56, pp. 247–307, 2008.

[51] L. Coldren and S. Corzine, *Diode lasers and photonic integrated circuits*. Wiley, 1995.

[52] G. New, "Pulse evolution in mode-locked quasi-continuous lasers," *IEEE J. of Quantum Electron.*, vol. 10, no. 2, pp. 115–124, 1974.

[53] H. Haus, "Theory of mode locking with a slow saturable absorber," *IEEE J. of Quantum Electron.*, vol. 11, no. 9, pp. 736–746, 1975.

[54] A. G. Vladimirov and D. Turaev, "Model for passive mode locking in semiconductor lasers," *Phys. Rev. A*, vol. 72, no. 3, p. 033808, 2005.

[55] E. A. Viktorov, P. Mandel, A. G. Vladimirov, and U. Bandelow, "Model for mode locking in quantum dot lasers," *Appl. Phys. Lett.*, vol. 88, no. 20, pp. 201 102–3, 2006.

[56] A. G. Vladimirov, U. Bandelow, G. Fiol, D. Arsenijevi, M. Kleinert, D. Bimberg, A. Pimenov, and D. Rachinskii, "Dynamical regimes in a monolithic passively mode-locked quantum dot laser," *J. Opt. Soc. Am. B*, vol. 27, no. 10, pp. 2102–2109, 2010.

[57] U. Bandelow, M. Radziunas, A. Vladimirov, B. Httl, and R. Kaiser, "40 GHz mode-locked semiconductor lasers: Theory, simulations and experiment," *Opt. Quantum Electron.*, vol. 38, no. 4-6, pp. 495–512, 2006.

[58] M. Rossetti, P. Bardella, and I. Montrosset, "Modeling passive mode-locking in quantum dot lasers: A comparison between a finite-difference traveling-wave model and a delayed differential equation approach," *IEEE J. of Quantum Electron.*, vol. 47, no. 5, pp. 569–576, 2011.

[59] ——, "Time-domain travelling-wave model for quantum dot passively mode-locked lasers," *IEEE J. of Quantum Electron.*, vol. 47, no. 2, pp. 139–150, 2011.

[60] J. Gomis-Bresco, S. Dommers, V. V. Temnov, U. Woggon, J. Martinez-Pastor, M. Laemmlin, and D. Bimberg, "InGaAs quantum dots coupled to a reservoir of nonequilibrium free carriers," *IEEE J. of Quantum Electron.*, vol. 45, no. 9, pp. 1121–1128, 2009.

[61] P. Borri, W. Langbein, J. M. Hvam, F. Heinrichsdorff, M. H. Mao, and D. Bimberg, "Spectral hole-burning and carrier-heating dynamics in InGaAs quantum-dot amplifiers," *IEEE J. Select. Top. Quantum Electron.*, vol. 6, no. 3, pp. 544–551, 2000.

[62] X. Huang, A. Stintz, H. Li, L. F. Lester, J. Cheng, and K. J. Malloy, "Passive mode-locking in 1.3 μm two-section InAs quantum dot lasers," *Appl. Phys. Lett.*, vol. 78, no. 19, pp. 2825–2827, 2001.

[63] X. Mo, M. G. Thompson, R. V. Penty, and I. H. White, "External-cavity mode-locked quantum-dot laser diodes for low repetition rate, sub-picosecond pulse generation," *IEEE J. Select. Top. Quantum Electron.*, vol. 17, no. 5, pp. 1264–1271, 2011.

[64] A. R. Rae, M. G. Thompson, R. V. Penty, I. H. White, A. R. Kovsh, S. S. Mikhrin, D. A. Livshits, and I. L. Krestnikov, "Harmonic mode-locking of a quantum-dot laser diode," in *Proc. 2006 IEEE LEOS Annu. Meeting Conf.*, pp. 874–875.

[65] M. G. Thompson, R. V. Penty, and I. H. White, "Regimes of mode-locking in tapered quantum dot laser diodes," in *Proc. Semicond. Laser Conf. (ISLC), Sorrento, Italy*, pp. 27–28.

[66] E. U. Rafailov, M. A. Cataluna, W. Sibbett, N. D. Il'inskaya, Y. M. Zadiranov, A. E. Zhukov, V. M. Ustinov, D. A. Livshits, A. R. Kovsh, and N. N. Ledentsov, "High-power picosecond and femtosecond pulse generation from a two-section mode-locked quantum-dot laser," *Appl. Phys. Lett.*, vol. 87, no. 8, pp. 081 107–3, 2005.

[67] M. G. Thompson, A. Rae, R. L. Sellin, C. Marinelli, R. V. Penty, I. H. White, A. R. Kovsh, S. S. Mikhrin, D. A. Livshits, and I. L. Krestnikov, "Subpicosecond high-power mode locking using flared waveguide monolithic quantum-dot lasers," *Appl. Phys. Lett.*, vol. 88, no. 13, pp. 133 119–3, 2006.

[68] D. Nikitichev, Y. Ding, M. Cataluna, E. Rafailov, L. Drzewietzki, S. Breuer, W. Elsaesser, M. Rossetti, P. Bardella, T. Xu, I. Montrosset, I. Krestnikov, D. Livshits, M. Ruiz, M. Tran, Y. Robert, and M. Krakowski, "High peak power and sub-picosecond fourier-limited pulse generation from passively mode-locked monolithic two-section gain-guided tapered InGaAs quantum-dot lasers," *Laser Phys.*, vol. 22, no. 4, pp. 715–724, 2012.

[69] E. A. Avrutin, J. H. Marsh, and E. L. Portnoi, "Monolithic and multi-gigahertz mode-locked semiconductor lasers: constructions, experiments, models and applications," *IET Optoelectron.*, vol. 147, no. 4, pp. 251–278, 2000.

[70] Y. Ding, R. Aviles-Espinosa, M. A. Cataluna, D. Nikitichev, M. Ruiz, M. Tran, Y. Robert, A. Kapsalis, H. Simos, C. Mesaritakis, T. Xu, P. Bardella, M. Rossetti, I. Krestnikov, D. Livshits, I. Montrosset, D. Syvridis, M. Krakowski, P. Loza-Alvarez, and E. Rafailov, "High peak-power picosecond pulse generation at 1.26 μm using a quantum-dot-based external-cavity mode-locked laser and tapered optical amplifier," *Opt. Express*, vol. 20, no. 13, pp. 14 308–14 320, 2012.

[71] H. A. Haus, "Theory of mode locking with a fast saturable absorber," *J. Appl. Phys.*, vol. 46, no. 7, pp. 3049–3058, 1975.

[72] R. G. M. P. Koumans and R. Van Roijen, "Theory for passive mode-locking in semiconductor laser structures including the effects of self-phase modulation, dispersion, and pulse collisions," *IEEE J. of Quantum Electron.*, vol. 32, no. 3, pp. 478–492, 1996.

[73] H. Haug and S. Koch, *Quantum Theory of the Optical and Electronic Properties of Semiconductors*. World Scientific, 2004.

[74] M. Rossetti, T. Xu, P. Bardella, and I. Montrosset, "Impact of gain saturation on passive mode locking regimes in quantum dot lasers with straight and tapered waveguides," *IEEE J. of Quantum Electron.*, vol. 47, no. 11, pp. 1404–1413, 2011.

[75] J. X. Chen, A. Markus, A. Fiore, U. Oesterle, R. P. Stanley, J. F. Carlin, R. Houdre, M. Ilegems, L. Lazzarini, L. Nasi, M. T. Todaro, E. Piscopiello, R. Cingolani, M. Catalano, J. Katcki, and J. Ratajczak, "Tuning InAs/GaAs quantum dot properties under stranski-krastanov growth mode for 1.3 μm applications," *J. Appl. Phys.*, vol. 91, no. 10, pp. 6710–6716, 2002.

[76] A. Kovsh, I. Krestnikov, D. Livshits, S. Mikhrin, J. Weimert, and A. Zhukov, "Quantum dot laser with 75nm broad spectrum of emission," *Opt. Lett.*, vol. 32, no. 7, pp. 793–795, 2007.

[77] K. A. Fedorova, M. A. Cataluna, I. Krestnikov, D. Livshits, and E. U. Rafailov, "Broadly tunable high-power InAs/GaAs quantum-dot external cavity diode lasers," *Opt. Express*, vol. 18, no. 18, pp. 19 438–19 443, 2010.

[78] A. Nevsky, U. Bressel, I. Ernsting, C. Eisele, M. Okhapkin, S. Schiller, A. Gubenko, D. Livshits, S. Mikhrin, I. Krestnikov, and A. Kovsh, "A narrow-line-width external cavity quantum dot laser for high-resolution spectroscopy in the near-infrared and yellow spectral ranges," *Appl. Phys. B-Lasers Opt.*, vol. 92, no. 4, pp. 501–507, 2008.

[79] B. Paola, S. Stephan, L. Wolfgang, and B. Dieter, "Ultrafast carrier dynamics in InGaAs quantum dot materials and devices," *Journal of Optics A: Pure and Applied Optics*, vol. 8, no. 4, p. S33, 2006.

[80] K. Yvind, D. Larsson, J. Mork, J. M. Hvam, M. Thompson, R. Penty, and I. White, "Low-noise monolithic mode-locked semiconductor lasers through low-dimensional structures," A. A. Belyanin and P. M. Smowton, Eds., vol. 6909. SPIE, pp. 69 090A–9.

[81] M.-T. Choi, J.-M. Kim, W. Lee, and P. J. Delfyett, "Ultralow noise optical pulse generation in an actively mode-locked quantum-dot semiconductor laser," *Appl. Phys. Lett.*, vol. 88, no. 13, pp. 131 106–3, 2006.

[82] T. W. Berg and J. Mork, "Quantum dot amplifiers with high output power and low noise," *Appl. Phys. Lett.*, vol. 82, no. 18, pp. 3083–3085, 2003.

[83] Y. C. Xin, L. Yan, A. Martinez, T. J. Rotter, S. Hui, Z. Lei, A. L. Gray, S. Luong, K. Sun, Z. Zou, J. Zilko, P. M. Varangis, and L. F. Lester, "Optical gain and absorption of quantum dots measured using an

alternative segmented contact method," *IEEE J. of Quantum Electron.*, vol. 42, no. 7, pp. 725–732, 2006.

[84] H. Saito, K. Nishi, A. Kamei, and S. Sugou, "Low chirp observed in directly modulated quantum dot lasers," *IEEE Photonics Technol. Lett.*, vol. 12, no. 10, pp. 1298–1300, 2000.

[85] L. A. Jiang, M. E. Grein, H. A. Haus, and E. P. Ippen, "Noise of mode-locked semiconductor lasers," *IEEE J. Select. Top. Quantum Electron.*, vol. 7, no. 2, pp. 159–167, 2001.

[86] A. Martinez, A. Lemaitre, K. Merghem, L. Ferlazzo, C. Dupuis, A. Ramdane, J. G. Provost, B. Dagens, O. Le Gouezigou, and O. Gauthier-Lafaye, "Static and dynamic measurements of the alpha-factor of five-quantum-dot-layer single-mode lasers emitting at 1.3 μm on GaAs," *Appl. Phys. Lett.*, vol. 86, no. 21, pp. 211 115–3, 2005.

[87] A. A. Ukhanov, A. Stintz, P. G. Eliseev, and K. J. Malloy, "Comparison of the carrier induced refractive index, gain, and linewidth enhancement factor in quantum dot and quantum well lasers," *Appl. Phys. Lett.*, vol. 84, no. 7, pp. 1058–1060, 2004.

[88] C. Y. Lin, Y. C. Xin, Y. Li, F. L. Chiragh, and L. F. Lester, "Cavity design and characteristics of monolithic long-wavelength InAs/InP quantum dash passively mode-locked lasers," *Opt. Express*, vol. 17, no. 22, pp. 19 739–19 748, 2009.

[89] A. R. Rae, M. G. Thompson, A. R. Kovsh, R. V. Penty, and I. H. White, "InGaAs-GaAs quantum-dot mode-locked laser diodes: Optimization of the laser geometry for subpicosecond pulse generation," *IEEE Photonics Technol. Lett.*, vol. 21, no. 5, pp. 307–309, 2009.

[90] L. Borruel, S. Sujecki, P. Moreno, J. Wykes, M. Krakowski, B. Sumpf, P. Sewell, S. C. Auzanneau, H. Wenzel, D. Rodriguez, T. M. Benson, E. C. Larkins, and I. Esquivias, "Quasi-3-D simulation of high-brightness tapered lasers," *IEEE J. of Quantum Electron.*, vol. 40, no. 5, pp. 463–472, 2004.

[91] D. W. Reschner, E. Gehrig, and O. Hess, "Pulse amplification and spatio-spectral hole-burning in inhomogeneously broadened quantum-dot semiconductor optical amplifiers," *IEEE J. of Quantum Electron.*, vol. 45, no. 1, pp. 21–33, 2009.

[92] L. Yan, M. Breivik, F. Cheng-Yong, B. O. Fimland, and L. F. Lester, "A low repetition rate all-active monolithic passively mode-locked quantum-dot laser," *IEEE Photonics Technol. Lett.*, vol. 23, no. 14, pp. 1019–1021, 2011.

[93] J. Palaski and K. Y. Lau, "Parameter ranges for ultrahigh frequency mode locking of semiconductor lasers," *Appl. Phys. Lett.*, vol. 59, no. 1, pp. 7–9, 1991.

[94] N. G. Usechak, X. Yongchun, L. Chang-Yi, L. F. Lester, D. J. Kane, and V. Kovanis, "Modeling and direct electric-field measurements of passively mode-locked quantum-dot lasers," *IEEE J. Select. Top. Quantum Electron.*, vol. 15, no. 3, pp. 653–660, 2009.

[95] Y. C. Xin, Y. Li, V. Kovanis, A. L. Gray, L. Zhang, and L. F. Lester, "Reconfigurable quantum dot monolithic multisection passive mode-locked lasers," *Opt. Express*, vol. 15, no. 12, pp. 7623–7633, 2007.

[96] D. Nikitichev, Y. Ding, M. Ruiz, M. Calligaro, N. Michel, M. Krakowski, I. Krestnikov, D. Livshits, M. Cataluna, and E. Rafailov, "High-power passively mode-locked tapered InAs/GaAs quantum-dot lasers," *Appl. Phys. B-Lasers Opt.*, vol. 103, no. 3, pp. 609–613, 2011.

[97] M. G. Thompson, A. R. Rae, R. V. Penty, I. H. White, A. R. Kovsh, S. S. Mikhrin, D. A. Livshits, and I. L. Krestnikov, "Absorber length optimisation for sub-picosecond pulse generation and ultra-low jitter performance in passively mode-locked 1.3 μm quantum-dot laser diodes," in *Optical Fiber Communication Conference, OFC 2006*, p. 3 pp.

[98] J. Javaloyes and S. Balle, "Anticolliding design for monolithic passively mode-locked semiconductor lasers," *Opt. Lett.*, vol. 36, no. 22, pp. 4407–4409, 2011.

[99] E. A. Viktorov, M. A. Cataluna, L. O'Faolain, T. F. Krauss, W. Sibbett, E. U. Rafailov, and P. Mandel, "Dynamics of a two-state quantum dot laser with saturable absorber," *Appl. Phys. Lett.*, vol. 90, no. 12, pp. 121 113–3, 2007.

[100] J. Liu, Z. Lu, S. Raymond, P. J. Poole, P. J. Barrios, and D. Poitras, "Dual-wavelength 92.5 GHz self-mode-locked inp-based quantum dot laser," *Opt. Lett.*, vol. 33, no. 15, pp. 1702–1704, 2008.

[101] L. Olejniczak, K. Panajotov, S. Wieczorek, H. Thienpont, and M. Sciamanna, "Intrinsic gain switching in optically injected quantum dot laser lasing simultaneously from the ground and excited state," *J. Opt. Soc. Am. B*, vol. 27, no. 11, pp. 2416–2423, 2010.

[102] S. Breuer, M. Rossetti, W. Elsasser, L. Drzewietzki, P. Bardella, I. Montrosset, M. Krakowski, and M. Hopkinson, "Reverse-emission-state-transition mode locking of a two-section InAs/InGaAs quantum dot laser," *Appl. Phys. Lett.*, vol. 97, no. 7, pp. 071 118–071 118–3, 2010.

[103] S. Breuer, M. Rossetti, L. Drzewietzki, P. Bardella, I. Montrosset, and W. Elsasser, "Joint experimental and theoretical investigations of two-state mode locking in a strongly chirped reverse-biased monolithic quantum dot laser," *IEEE J. of Quantum Electron.*, vol. 47, no. 10, pp. 1320–1329, 2011.

[104] M. A. Cataluna, D. I. Nikitichev, S. Mikroulis, H. Simos, C. Simos, C. Mesaritakis, D. Syvridis, I. Krestnikov, D. Livshits, and E. U. Rafailov, "Dual-wavelength mode-locked quantum-dot laser, via ground and excited state transitions: experimental and theoretical investigation," *Opt. Express*, vol. 18, no. 12, pp. 12 832–12 838, 2010.

[105] A. V. Uskov, T. W. Berg, and J. Mrk, "Theory of pulse-train amplification without patterning effects in quantum-dot semiconductor optical amplifiers," *IEEE J. of Quantum Electron.*, vol. 40, no. 3, pp. 306–320, 2004.

[106] K. Okamoto, *Fundamentals of Optical Waveguides*. Elsevier, 2006.

[107] L. Jie-Wei and L. Ching-Fuh, "Carrier diffusion effect in tapered semiconductor-laser amplifier," *IEEE J. of Quantum Electron.*, vol. 34, no. 7, pp. 1247–1256, 1998.

[108] S. Balsamo, F. Sartori, and I. Montrosset, "Dynamic beam propagation method for flared semiconductor power amplifiers," *IEEE J. Select. Top. Quantum Electron.*, vol. 2, no. 2, pp. 378–384, 1996.

[109] Y. Ben-Ezra, M. Haridim, and B. I. Lembrikov, "Theoretical analysis of gain-recovery time and chirp in QD-SOA," *IEEE Photonics Technol. Lett.*, vol. 17, no. 9, pp. 1803–1805, 2005.

[110] X. Jin-Long and H. Yong-Zhen, "Numerical analysis of gain saturation, noise figure, and carrier distribution for quantum-dot semiconductor-optical amplifiers," *IEEE J. of Quantum Electron.*, vol. 44, no. 5, pp. 448–455, 2008.

[111] K. A. Williams, R. V. Penty, I. H. White, D. J. Robbins, F. J. Wilson, J. I. Lewandowski, and B. K. Nayar, "Design of high-brightness tapered laser arrays," *IEEE J. Select. Top. Quantum Electron.*, vol. 5, no. 3, pp. 822–831, 1999.

[112] O. Qasaimeh, "Optical gain and saturation characteristics of quantum-dot semiconductor optical amplifiers," *IEEE J. of Quantum Electron.*, vol. 39, no. 6, pp. 793–798, 2003.

[113] W. W. Chow, H. Amano, and I. Akasaki, "Theoretical analysis of filamentation and fundamental-mode operation in InGaN quantum well lasers," *Appl. Phys. Lett.*, vol. 76, no. 13, pp. 1647–1649, 2000.

[114] D. Scholz, H. Braun, U. T. Schwarz, S. Brninghoff, D. Queren, A. Lell, and U. Strauss, "Measurement and simulation of filamentation in (Al,In)GaN laser diodes," *Opt. Express*, vol. 16, no. 10, pp. 6846–6859, 2008.

[115] D. Yevick, "A guide to electric field propagation techniques for guided-wave optics," *Opt. Quantum Electron.*, vol. 26, no. 3, pp. S185–S197, 1994.

[116] G. R. Hadley, "Transparent boundary condition for the beam propagation method," *IEEE J. of Quantum Electron.*, vol. 28, no. 1, pp. 363–370, 1992.

[117] T. Akiyama, M. Ekawa, M. Sugawara, K. Kawaguchi, S. Hisao, A. Kuramata, H. Ebe, and Y. Arakawa, "An ultrawide-band semiconductor optical amplifier having an extremely high penalty-free output power of 23 dBm achieved with quantum dots," *IEEE Photonics Technol. Lett.*, vol. 17, no. 8, pp. 1614–1616, 2005.

[118] N. J. Kim, J. M. Oh, M. D. Kim, D. Lee, S. H. Pyun, W. G. Jeong, and J. W. Jang, "Gain characteristics of InAs/InGaAsP quantum dot semiconductor optical amplifiers at 1.5 μm," *Appl. Phys. Lett.*, vol. 90, no. 24, pp. 241 108–3, 2007.

[119] J. N. Walpole, E. S. Kintzer, S. R. Chinn, C. A. Wang, and L. J. Missaggia, "High-power strained-layer InGaAs/AlGaAs tapered traveling wave amplifier," *Appl. Phys. Lett.*, vol. 61, no. 7, pp. 740–742, 1992.

[120] A. E. Siegman, "How to (maybe) measure laser beam quality," ser. OSA Trends in Optics and Photonics, M. Dowley, Ed., vol. 17. Optical Society of America, p. MQ1.

[121] J. Niu and J. Xu, "Coupling efficiency of laser beam to multimode fiber," *Opt. Commun.*, vol. 274, no. 2, pp. 315–319, 2007.

[122] J. R. Marciante and G. P. Agrawal, "Nonlinear mechanisms of filamentation in broad-area semiconductor lasers," *IEEE J. of Quantum Electron.*, vol. 32, no. 4, pp. 590–596, 1996.

Journal publications

[1] T. Xu, P. Bardella, M. Rossetti, and I. Montrosset, "Beam propagation method simulation and analysis of quantum dot flared semiconductor optical amplifiers in continuous wave high-saturation regime," *IET Optoelectron.*, vol. 6, no. 2, pp. 110–116, 2012.

[2] T. Xu, M. Rossetti, P. Bardella, and I. Montrosset, "Simulation and analysis of dynamic regimes involving ground and excited state transitions in quantum dot passively mode-locked lasers," *IEEE J. of Quantum Electron.*, vol. 48, no. 9, pp. 1193–1202, 2012.

[3] T. Xu, P. Bardella, and I. Montrosset, "Cavity optimization of quantum dot passively mode-locked lasers for high power and short pulse generation," *IEEE Photonics Technol. Lett.*, vol. 25, no. 1, pp. 63–66, 2013.

[4] T. Xu and I. Montrosset, "Quantum dot passively mode-locked lasers: Relation between intracavity pulse evolution and mode locking performances," *IEEE J. of Quantum Electron.*, vol. 49, no. 1, pp. 65–71, 2013.

[5] M. Rossetti, T. Xu, P. Bardella, and I. Montrosset, "Impact of gain saturation on passive mode locking regimes in quantum dot lasers with straight and tapered waveguides," *IEEE J. of Quantum Electron.*, vol. 47, no. 11, pp. 1404–1413, 2011.

[6] Y. Ding, R. Aviles-Espinosa, M. A. Cataluna, D. Nikitichev, M. Ruiz, M. Tran, Y. Robert, A. Kapsalis, H. Simos, C. Mesaritakis, T. Xu, P. Bardella, M. Rossetti, I. Krestnikov, D. Livshits, I. Montrosset, D. Syvridis, M. Krakowski, P. Loza-Alvarez, and E. Rafailov, "High peak-power picosecond pulse generation at 1.26 μm using a quantum-dot-based external-cavity mode-locked laser and tapered optical amplifier," *Opt. Express*, vol. 20, no. 13, pp. 14 308–14 320, 2012.

[7] D. Nikitichev, Y. Ding, M. Cataluna, E. Rafailov, L. Drzewietzki, S. Breuer, W. Elsaesser, M. Rossetti, P. Bardella, T. Xu, I. Montrosset, I. Krestnikov, D. Livshits, M. Ruiz, M. Tran, Y. Robert, and

M. Krakowski, "High peak power and sub-picosecond fourier-limited pulse generation from passively mode-locked monolithic two-section gain-guided tapered InGaAs quantum-dot lasers," *Laser Phys.*, vol. 22, no. 4, pp. 715–724, 2012.

[8] M. Rossetti, T. Xu, P. Bardella, and I. Montrosset, "Modelling of passive mode-locking in InAs quantum-dot lasers with tapered gain section," *Phys. Status Solidi (c)*, vol. 9, no. 2, pp. 286–289, 2012.

[9] Y. Ding, A. Alhazime, D. Nikitichev, K. Fedorova, M. Ruiz, M. Tran, Y. Robert, A. Kapsalis, H. Simos, C. Mesaritakis, T. Xu, P. Bardella, M. Rossetti, I. Krestnikov, D. Livshits, I. Montrosset, D. Syvridis, M. A. Cataluna, M. Krakowski, and E. Rafailov, "Tunable master-oscillator power-amplifier based on chirped quantum-dot structures," *IEEE Photonics Technol. Lett.*, vol. 24, no. 20, pp. 1841–1844, 2012.

[10] H. Simos, M. Rossetti, C. Simos, C. Mesaritakis, T. Xu, P. Bardella, I. Montrosset, and D. Syvridis, "Numerical analysis of passively mode-locked quantum-dot lasers with absorber section at the low-reflectivity output facet," *IEEE J. of Quantum Electron.*, vol. 49, no. 1, pp. 3–10, 2013.